

SN 2016coi (ASASSN-16fp): AN ENERGETIC H-STRIPPED CORE-COLLAPSE SUPERNOVA FROM A MASSIVE STELLAR PROGENITOR WITH LARGE MASS LOSS

G. TERRERAN,¹ R. MARGUTTI,¹ D. BERSIER,² J. BRIMACOMBE,³ D. CAPRIOLI,⁴ P. CHALLIS,⁵ R. CHORNOCK,⁶ D. L. COPPEJANS,¹ SUBO DONG,⁷ C. GUIDORZI,⁸ K. HURLEY,⁹ R. KIRSHNER,⁵ G. MIGLIORI,^{10,11} D. MILISAVLJEVIC,¹² D. M. PALMER,¹³ J. L. PRIETO,^{14,15} L. TOMASELLA,¹⁶ P. MARCHANT,¹ A. PASTORELLO,¹⁶ B. J. SHAPPEE,¹⁷ K. Z. STANEK,^{18,19} M. D. STRITZINGER,²⁰ S. BENETTI,¹⁶ PING CHEN,⁷ L. DEMARCHI,¹ N. ELIAS-ROSA,^{21,22} C. GALL,²³ J. HARMANEN,²⁴ AND S. MATTILA²⁴

¹Center for Interdisciplinary Exploration and Research in Astrophysics (CIERA) and Department of Physics and Astronomy, Northwestern University, Evanston, IL 60208

²Astrophysics Research Institute, Liverpool John Moores University, 146 Brownlow Hill, Liverpool L3 5RF, UK

³Coral Towers Observatory, Cairns, QLD 4870, Australia

⁴Department of Astrophysical Sciences, Princeton University, 4 Ivy Ln., Princeton NJ 08544, USA

⁵Harvard-Smithsonian Center for Astrophysics, 60 Garden Street, Cambridge, Massachusetts, 02138, USA

⁶Astrophysical Institute, Department of Physics and Astronomy, 251B Clippinger Lab, Ohio University, Athens, OH 45701, USA

⁷Kavli Institute for Astronomy and Astrophysics, Peking University, Yi He Yuan Road 5, Hai Dian District, Beijing 100871, China

⁸Department of Physics and Earth Science, University of Ferrara, via Saragat 1, I-44122, Ferrara, Italy

⁹University of California, Berkeley, Space Sciences Laboratory, 7 Gauss Way, Berkeley, CA 94720-7450, USA

¹⁰Dipartimento di Fisica e Astronomia, Alma Mater Studiorum, Università degli Studi di Bologna, Via Gobetti 93/2, I-40129 Bologna, Italy

¹¹INAF Istituto di Radioastronomia, via Gobetti 101, I-40129 Bologna, Italy

¹²Department of Physics and Astronomy, Purdue University, 525 Northwestern Avenue, West Lafayette, IN 47906, USA

¹³Los Alamos National Laboratory, Los Alamos, NM, 87545, USA

¹⁴Núcleo de Astronomía de la Facultad de Ingeniería, Universidad Diego Portales, Av. Ejército 441, Santiago, Chile

¹⁵Millennium Institute of Astrophysics, Santiago, Chile

¹⁶INAF–Osservatorio Astronomico di Padova, vicolo dell’Osservatorio 5, Padova I-35122, Italy

¹⁷Institute for Astronomy, University of Hawai’i, 2680 Woodlawn Drive, Honolulu, HI 96822, USA

¹⁸Department of Astronomy, The Ohio State University, 140 West 18th Avenue, Columbus, OH 43210, USA

¹⁹Center for Cosmology and Astroparticle Physics, The Ohio State University, 191 W. Woodruff Avenue, Columbus, OH 43210, USA

²⁰Department of Physics and Astronomy, Aarhus University, Ny Munkegade 120, 8000 Aarhus C, Denmark

²¹Institute of Space Sciences (ICE, CSIC), Campus UAB, Carrer de Can Magrans s/n, 08193 Barcelona, Spain

²²Institut d’Àlgebra i Estudis Espacials de Catalunya (IEEC), c/Gran Capitá 2-4, Edif. Nexus 201, 08034 Barcelona, Spain

²³DARK, Niels Bohr Institute, University of Copenhagen, Lyngbyvej 2, 2100 Copenhagen, Denmark

²⁴Tuorla Observatory, Department of Physics and Astronomy, FI-20014 University of Turku, Finland

Submitted to ApJ

ABSTRACT

We present comprehensive observations and analysis of the energetic H-stripped SN 2016coi (a.k.a. ASASSN-16fp), spanning the γ -ray through optical and radio wavelengths, acquired within the first hours to ~ 420 days post explosion. Our observational campaign confirms the identification of He in the SN ejecta, which we interpret to be caused by a larger mixing of Ni into the outer ejecta layers. From the modeling of the broad bolometric light curve we derive a large ejecta mass to kinetic energy ratio ($M_{\text{ej}} \sim 4-7 M_{\odot}$, $E_{\text{k}} \sim 7-8 \times 10^{51}$ erg). The small [Ca II] $\lambda\lambda 7291, 7324$ to [O I] $\lambda\lambda 6300, 6364$ ratio (~ 0.2) observed in our late-time optical spectra is suggestive of a large progenitor core mass at the time of collapse. We find that SN 2016coi is a luminous source of X-rays ($L_{\text{X}} > 10^{39}$ erg s⁻¹ in the first ~ 100 days post explosion) and radio emission ($L_{8.5 \text{ GHz}} \sim 7 \times 10^{27}$ erg s⁻¹ Hz⁻¹ at peak). These values are in line with those of relativistic SNe (2009bb, 2012ap). However, for SN 2016coi we infer substantial

pre-explosion progenitor mass-loss with rate $\dot{M} \sim (1-2) \times 10^{-4} M_{\odot} \text{yr}^{-1}$ and a sub-relativistic shock velocity $v_{sh} \sim 0.15c$, in stark contrast with relativistic SNe and similar to normal SNe. Finally, we find no evidence for a SN-associated shock breakout γ -ray pulse with energy $E_{\gamma} > 2 \times 10^{46}$ erg. While we cannot exclude the presence of a companion in a binary system, taken together, our findings are consistent with a massive single star progenitor that experienced large mass loss in the years leading up to core-collapse, but was unable to achieve complete stripping of its outer layers before explosion.

Keywords: supernovae, SN 2016coi, ASASSN-16fp

1. INTRODUCTION

Hydrogen-stripped core-collapse supernovae (i.e., type Ibc SNe), also called stripped-envelope SNe (SESNe; [Clocchiatti et al. 1996](#)), have enjoyed a surge of interest in the last two decades thanks to the association of the most energetic elements of the class with Gamma-Ray Bursts (GRBs). Yet, the stellar progenitors of type Ibc SNe have so far eluded uncontroversial detection in pre-explosion images ([Gal-Yam et al. 2005](#); [Maund et al. 2005](#); [Elias-Rosa et al. 2013](#); [Eldridge et al. 2013](#)). Relevant in this respect is the discovery of a progenitor in pre-explosion images of the type Ib SN iPTF13bvn, interpreted to be a single Wolf-Rayet (WR) star with a mass at zero-age main-sequence (ZAMS) $M_{\text{ZAMS}} \sim 33 M_{\odot}$ ([Cao et al. 2013](#); [Groh et al. 2013](#)). This result was later disputed by [Bersten et al. \(2014a\)](#). More recently, [Van Dyk et al. \(2018\)](#), [Kilpatrick et al. \(2018\)](#) and [Xiang et al. \(2019\)](#) identified a source in archival *Hubble Space Telescope* (HST) images covering the location of the type Ic SN 2017ein, with properties compatible with a WR star of $M_{\text{ZAMS}} \sim 55 M_{\odot}$ (although the presence of a companion star could not be ruled out).

The stripping of the hydrogen and helium envelope in massive stars mainly occurs through two channels: (i) line-driven winds, which dominate the mass-loss yield in single star evolution; or (ii) interaction with a companion star in a binary system. In the former scenario, the progenitor is expected to be an isolated, massive WR star ($M_{\text{ZAMS}} \gtrsim 20 M_{\odot}$; [Hamann et al. 2006](#)), consistent with the inferences by [Cao et al. \(2013\)](#), [Groh et al. \(2013\)](#), [Van Dyk et al. \(2018\)](#) and [Kilpatrick et al. \(2018\)](#) with typical mass-loss rate $\dot{M} \sim 10^{-5} M_{\odot} \text{ yr}^{-1}$ ([Maeder 1981](#); [Woosley et al. 1995](#); [Begelman & Sarazin 1986](#)). In the binary progenitor scenario, instead, the primary exploding star is expected to be a helium star (or a C+O star in case of type Ic SNe) with lower-mass $M_{\text{ZAMS}} \gtrsim 12 M_{\odot}$ ([Podsiadlowski et al. 1992](#); [Yoon et al. 2010](#); [Eldridge et al. 2013](#); [Dessart et al. 2015](#)). The lower mass of the progenitor stars in the binary progenitor scenario naturally accounts for the discrepancy between the large inferred rate of SESNe compared to massive WR stars ([Georgy et al. 2009](#); [Smith et al. 2011](#); [Eldridge et al. 2013](#); [Smith 2014](#)), and for the low ejecta masses inferred from the modeling of the bolometric light-curves of type Ibc SNe ($M_{\text{ej}} \lesssim 3 M_{\odot}$; e.g., [Ensmann & Woosley 1988](#); [Drout et al. 2011](#); [Dessart et al. 2012](#); [Bersten et al. 2014b](#); [Eldridge et al. 2015](#); [Lyman et al. 2016](#); [Taddia et al. 2018](#)). In reality, both scenarios are likely contributing in different amounts to the observed population of SESNe.

Here we present the results from an extensive multi-wavelength campaign of the H-poor SN 2016coi (a.k.a. ASASSN-16fp) from γ -rays to radio wavelengths, from a few hrs to ~ 420 days post explosion. From our comprehensive analysis we infer that SN 2016coi originated from

a compact massive progenitor with large mass loss before explosion, potentially consistent with a single WR progenitor star. SN 2016coi was discovered on 2016 May 27.55 UT ([Holoien et al. 2016](#), MJD 57535.55;) by the All Sky Automated Survey for SuperNovae¹ (ASAS-SN; [Shappee et al. 2014](#)) in the irregular galaxy UGC 11868 (Fig. 1). SN 2016coi was initially classified by the NOT Unbiased Transient Survey (NUTS; [Mattila et al. 2016](#)) as a type Ic-BL SN similar to those that accompany GRBs ([Elias-Rosa et al. 2016](#)), although it was soon realized that traces of He might have been present at early times ([Yamanaka et al. 2016](#)). The optical/UV properties of SN 2016coi have been studied by [Yamanaka et al. \(2017\)](#), [Prentice et al. \(2018\)](#) and [Kumar et al. \(2018\)](#). These authors conclude that SN 2016coi is an energetic SN with large ejecta mass and spectroscopic similarities to type Ic-BL SNe. In terms of SN classification, SN 2016coi is intermediate between type Ib and Ic SNe. Unlike type Ib SNe, where He lines become more prominent with time (e.g., [Gal-Yam 2017](#)), the He features of SN 2016coi disappear after maximum light.

This paper is organized as follows. We first describe our UV, optical and NIR photometry data analysis and derive the explosion properties through modeling of the SN bolometric emission in §2. Our spectroscopic campaign and inferences on the spectral properties of SN 2016coi are described in §3. In §4 we present radio observations of SN 2016coi, along with the modeling of the blast-wave synchrotron emission, while §5 is dedicated to the analysis of the luminous X-ray emission of SN 2016coi and the constraints on the progenitor mass-loss history. We describe our search for a shock breakout signal in the γ -rays in §6. We discuss our findings in the context of properties of potential stellar progenitors in §7 and draw our conclusions in §8.

In this paper we follow [Kumar et al. \(2018\)](#) and adopt $z \simeq 0.00365$, which corrected for Virgo infall corresponds to a distance of 18.1 ± 1.3 Mpc ($H_0 = 73 \text{ km s}^{-1} \text{ Mpc}^{-1}$, $\Omega_M = 0.27$, $\Omega_{\Lambda} = 0.73$), equivalent to a distance modulus of $\mu = 31.29 \pm 0.15$ mag ([Mould et al. 2000](#)). We further adopt a total color excess in the direction of SN 2016coi $E(B-V)_{\text{tot}} = 0.075$ mag ([Schlafly & Finkbeiner 2011](#)) as in [Yamanaka et al. \(2017\)](#) and [Kumar et al. \(2018\)](#). Unless otherwise stated, time is referred to the inferred time of first light (§2), which is UT May 23.9 2016 (MJD 57531.9; see §2.2). The presence of a “dark phase” with a duration of a few hours to a few days (e.g., [Piro & Nakar 2013](#)) has no impact on our major conclusions. Therefore we use the term “from explosion” and “from first light” interchangeably. A summary of our adopted and inferred parameters is provided in Table 1. Uncertainties are listed at the 1σ confidence level (c.l.),

¹ <http://www.astronomy.ohio-state.edu/~assassin/index.shtml>

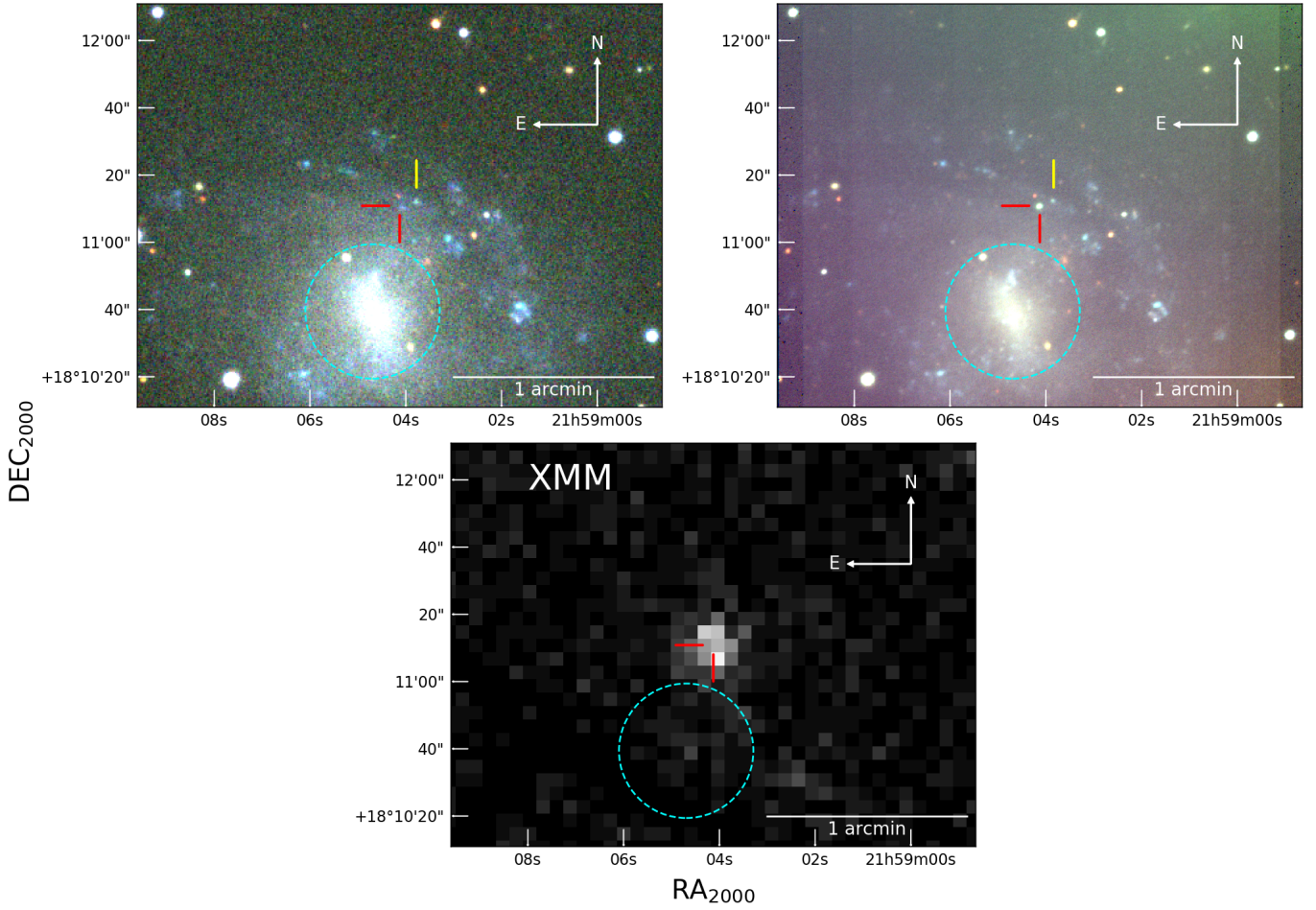


Figure 1. Optical (upper panels) and X-ray (lower panel) images of SN 2016coi and its surroundings. *Upper panels, left:* SDSS pre-explosion false-color image of the host galaxy UGC 11868 of SN 2016coi in the *gri* filters. Observations were acquired on 2009, October 16 UT. *Upper panels, right:* post-explosion false-color image based on *gri* observations acquired with MMTCam on 2017, June 02 UT (~ 1 yr post explosion). *Lower Panel:* 0.3–10 keV image from XMM-Newton observations at $t \leq 22$ days. In all panels the location of the SN is marked in red, a yellow mark indicates the location of a nearby H II region, while a dashed cyan circle with $20''$ radius identifies the host-galaxy center.

Table 1. Summary of assumed and inferred parameters from this paper and previous publications.

	Yamanaka et al. (2017)	Kumar et al. (2018)	Prentice et al. (2018)	This Work
Distance (modulus μ)	17.2 Mpc (31.18 mag)	18.1 Mpc (31.29 mag)	15.8 Mpc (31 mag)	18.1 Mpc (31.29 mag)
Color Excess $E(B-V)_{\text{tot}}$	0.075 mag	0.074 mag	0.205 mag	0.075 mag
Explosion Date	MJD 57532.5	MJD 57533.9	MJD 57533.5	MJD 57531.9
Nickel Mass M_{Ni}	$0.15 M_{\odot}$	$0.10 M_{\odot}$	$0.14 M_{\odot}$	$0.15 M_{\odot}$
Ejecta Mass M_{ej}	$10 M_{\odot}$	$4.5 M_{\odot}$	$2.4\text{--}4 M_{\odot}$	$4\text{--}7 M_{\odot}$
Kinetic Energy E_k	$3\text{--}5 \times 10^{52}$ erg	6.9×10^{51} erg	$4.5\text{--}7 \times 10^{51}$ erg	$7\text{--}8 \times 10^{51}$ erg
He Velocity	~ 18000 km s $^{-1}$	~ 20000 km s $^{-1}$	~ 22000 km s $^{-1}$	~ 22000 km s $^{-1}$

and upper limits are provided at the 3σ c.l. unless otherwise noted.

2. UV, OPTICAL AND NIR PHOTOMETRY

2.1. Data Analysis

Our photometric data have been obtained from several different telescopes and instruments, which are listed in Table A1. UV data have been acquired with the Ultraviolet Optical Telescope (UVOT; Roming et al. 2005), on the Neil Gehrels *Swift* Observatory (Gehrels et al. 2004). We measured the SN instrumental magnitudes by performing aperture photometry with the `uvotsource` task within the HEASOFT v6.22, and following the guidelines in Brown et al. (2009). An aperture of $3''$ was used. We estimated the level of contamination from the host galaxy flux using late-time observations acquired at $t \sim 322$ d after first light, when the SN contribution is negligible. We then subtracted the measured count-rate at the location of the SN from the count rates in the SN images following the prescriptions in Brown et al. (2014).

Images acquired with the Liverpool Telescope have been processed with a custom-made pipeline, while we use standard overscan, bias and flatfielding within IRAF² for the remaining optical photometry. NOTCam NIR images were reduced with a modified version of the external IRAF package IRAF (v. 2.5)³. The remaining NIR data reduction has been performed through standard flat-field correction, sky background subtraction and stacking of the individual exposures for an improved signal-to-noise ratio. The photometry has been extracted using the SNOOPY⁴ package. We performed point-spread-function (PSF) photometry with DAOPHOT (Stetson 1987). For non-detections we calculated upper limits corresponding to a S/N of 3. Zero points and color terms for each night have been estimated based on the magnitudes of field stars in the Sloan Digital Sky Survey⁵ (SDSS; York et al. 2000) catalog (DR9). We converted the SDSS *ugriz* magnitudes to Johnson/Cousins *UBVRI* filters following Chonis & Gaskell (2008). For NIR images, we used the Two Micron All Sky Survey (2MASS) catalog⁶ (Skrutskie et al. 2006). We quantified the uncertainty on the instrumental magnitude injecting artificial stars (e.g., Hu et al. 2011). The resulting uncertainty was then added in quadrature to the fit uncertainties returned by DAOPHOT

² IRAF is distributed by the National Optical Astronomy Observatory, which is operated by the Association of Universities for Research in Astronomy (AURA) under a cooperative agreement with the National Science Foundation. <http://iraf.noao.edu/>

³ <http://www.not.iac.es/instruments/notcam/guide/observe.html#reductions>

⁴ Cappellaro, E. (2014). SNOOPY: a package for SN photometry. <http://sngroup.oapd.inaf.it/snoopy.html>

⁵ <http://www.sdss.org>

⁶ <http://www.ipac.caltech.edu/2mass/>

and the uncertainties from the photometric calibration to obtain the total uncertainty on the photometry. Our final values are reported in Tables A2–A5 and shown in Fig. 2.

Our UV-to-NIR campaign densely samples the evolution of SN 2016coi in its first ~ 400 days post explosion, with more than 1100 observations distributed over 166 nights (the gap around 200–300 days corresponds to when SN 2016coi was behind to the Sun). As Fig. 2 shows, SN 2016coi rises to peak considerably faster in the bluer bands. The UV filters also show the fastest decline post peak, before relaxing on a significantly slower decay at $t \gtrsim 40$. This sharp change of decay rate is not present in the redder bands, which instead show a roughly constant decay rate after peak. The late-time *V*-band decays as $1.7 \text{ mag } 100\text{d}^{-1}$, faster than expected from the radioactive decay of ^{56}Co , suggesting leakage of γ -rays. Our last detections of SN 2016coi at ~ 373 d post explosion are consistent with the temporal decay inferred from earlier observations at $50\text{d} \lesssim t \lesssim 300\text{d}$ (Fig. 2). Finally, by using a low-order polynomial fit we measure the time of maximum light in the *V* band $V_{max} = 18.34 \pm 0.16$ d after discovery, corresponding to MJD 57550.24 (2016 June 11.24 UT). The time of peak in other bands is reported in Table A6.

2.2. Bolometric Luminosity and Explosion Parameters

Our extensive photometric coverage allows us to reconstruct the bolometric emission from SN 2016coi from the UV to the NIR from a few days to ~ 200 days after explosion. As a comparison, the bolometric light-curve from Prentice et al. (2018) has similar temporal coverage but does not include the NIR and UV contributions, while Kumar et al. (2018) and Yamanaka et al. (2017) include either the UV emission or the NIR emission until $\delta t \leq 60$ days post explosion, respectively. We build the bolometric luminosity curve of SN 2016coi starting from extinction-corrected flux densities, and we interpolate the flux densities in each filter to estimate the SN emission at any given time of interest. In case of incomplete UV-to-NIR photometric coverage we assume constant color from the previous closest epochs. Finally, we integrate the resulting spectral energy distributions (SEDs) from the UV to the NIR with the trapezoidal rule to obtain the bolometric light-curve shown in Fig. 3.

We compare the bolometric light curve of SN 2016coi with a sample of well-observed H-stripped core-collapse SNe from Lyman et al. (2016) in Fig. 3. Lyman et al. (2016) used the parameter Δ_{15} as an estimator of the broadness of the light curve, defined as the the difference in magnitude between the luminosity at peak at the luminosity 15 d after that. The smaller the Δ_{15} , the “slower” the event, i.e., the broader the light curve. The SN with the broadest light curve in the sample of Lyman et al. (2016) is the type-Ic SN 2011bm, which has $\Delta_{15} = 0.2$ mag. Other slow events are the type-Ic SNe 2004aw, 2005az (with $\Delta_{15} = 0.41$ and $\Delta_{15} = 0.42$ mag,

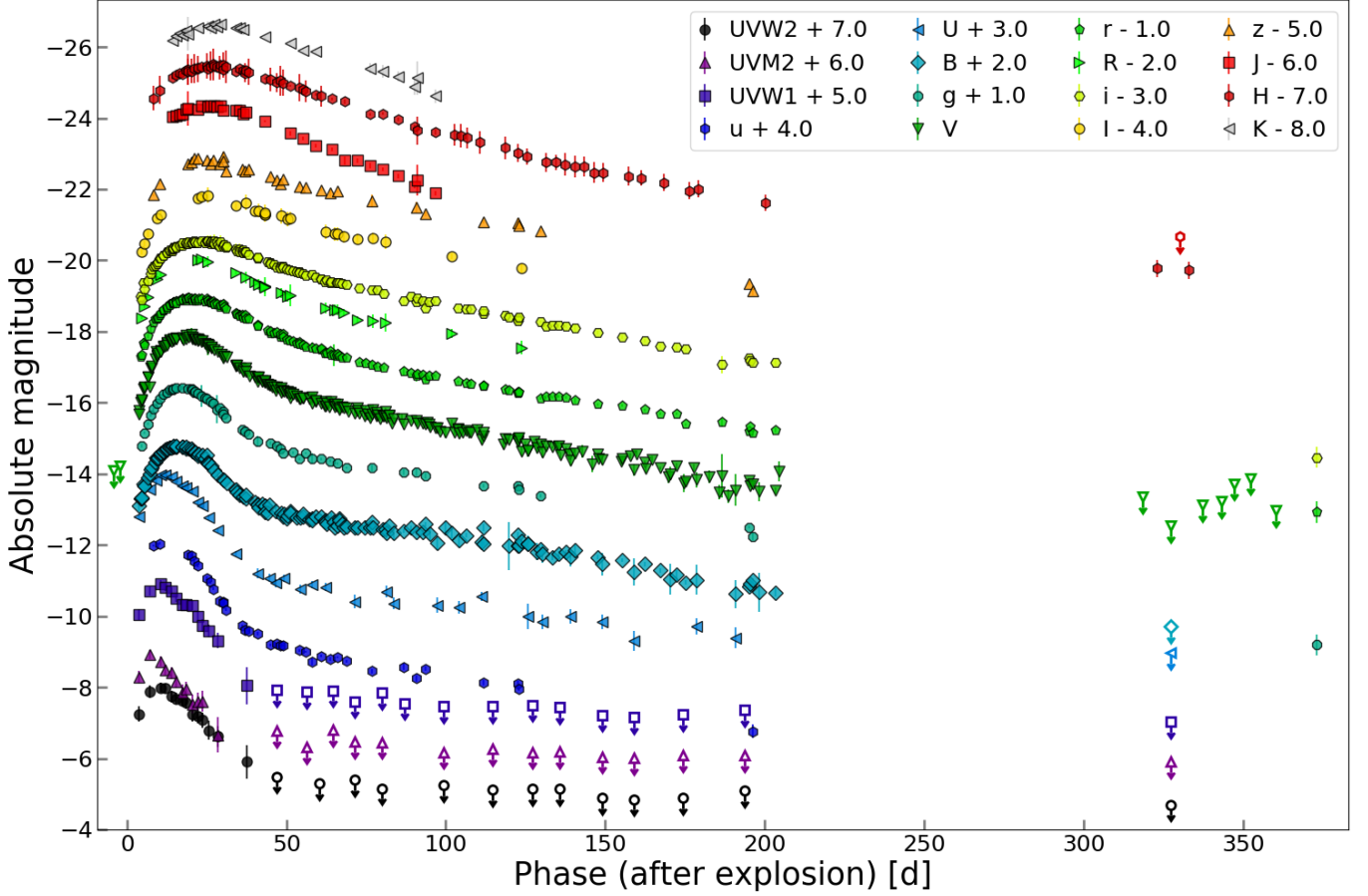


Figure 2. UV, optical and NIR emission from SN 2016coi in the first ~ 400 days of its evolution. We show extinction corrected absolute magnitudes. Upper limits are marked by empty symbols.

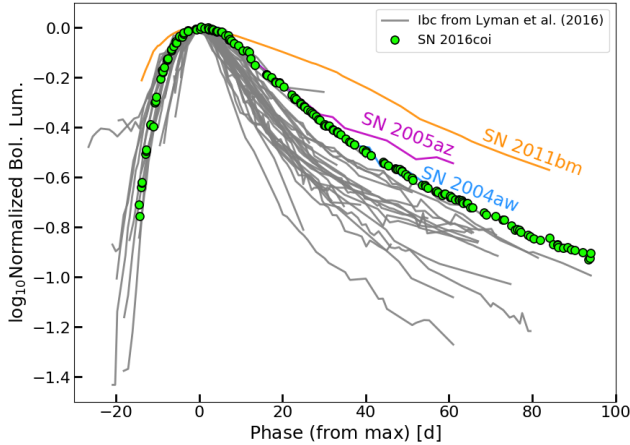


Figure 3. Comparison of the *uvoir* bolometric light curve of SN 2016coi with the sample of SESNe from Lyman et al. (2016). The light curves have been normalized to maximum light. SN 2016coi is among the objects with the broadest light curve, suggesting a larger than average diffusion time. The broad light curves of SNe 2004aw (which lies exactly below SN 2016coi; Taubenberger et al. 2006), 2005az (Drout et al. 2011) and 2011bm (Valenti et al. 2012) are also marked.

respectively) and the type-Ib SNe 1999dn and 2004dk (with $\Delta_{15}=0.32$ and $\Delta_{15}=0.41$ mag, respectively). Figure 3 shows that with $\Delta_{15}=0.41$ mag, SN 2016coi is among the SNe with the broadest light-curves. Kumar et al. (2018) did a similar analysis looking at the Δ_{15} in the single bands and reached the same conclusion.

The broad light curve indicates a large photon diffusion time scale, and hence a large ejecta mass (M_{ej}) to kinetic energy (E_k) ratio. Assuming standard energetics, this translates to a considerably large ejecta mass, in agreement with previous findings by Prentice et al. (2018) and Kumar et al. (2018). Interestingly, SN 2016coi shows a very slow post-peak decline with a standard time to peak $t_{rise} < 20$ days (Fig. 3). This phenomenology might result from mixing of ^{56}Ni in the outer stellar ejecta, as opposed of having all the ^{56}Ni located at the centre of the explosion. We quantify these statements below.

We model the bolometric light-curve of SN 2016coi adopting the formalism by Arnett (1982) modified following Valenti et al. (2008) and Wheeler et al. (2015). We adopt a mean opacity $\kappa_{opt} = 0.07 \text{ cm}^2 \text{ g}^{-1}$ and break the model degeneracy using a photospheric velocity $v_{phot} \sim 16000 \text{ km s}^{-1}$

around maximum light, as inferred from Fe II spectral lines (§3). We find that during the photospheric phase at $t < 30$ days the light-curve is well described by a model with kinetic energy $E_{k,phot} \sim 7 \times 10^{51}$ erg, ^{56}Ni mass $M_{Ni,phot} = 0.13 M_{\odot}$ and ejecta mass $M_{ej,phot} \sim 4 M_{\odot}$, consistent with the findings of Kumar et al. (2018). However, this model significantly underestimates the bolometric emission during the nebular phase. This is a common outcome of the modeling of energetic type-Ic SN light-curves, which motivated Maeda et al. (2003) and Valenti et al. (2008) to consider a two-component model. In two-component models the “outer component” dominates the early-time emission during the photospheric phase, while the late-time nebular emission receives a significant contribution from a denser inner core (“inner component”). Applying this modeling we find a total ejecta mass $M_{ej} \sim (4-7) M_{\odot}$, $E_k \sim (7-8) \times 10^{51}$ erg and $M_{Ni} \sim 0.15 M_{\odot}$, with a larger fraction of Ni per unit mass in the outer component. This model also allows us to constrain the time of first light to MJD 57531.9 ± 1.5 days (May 23.9, 2016 UT).

As a comparison, the spectral modeling by Prentice et al. (2018) indicates $M_{ej} = 2.4-4 M_{\odot}$, $E_k = (4.5-7) \times 10^{51}$ erg. Scaling the emission of SN 2016coi to the GRB-associated SN 2006aj and SN 2008D, Yamanaka et al. (2017) find $M_{ej} \sim 10 M_{\odot}$, $E_k = (3-5) \times 10^{52}$ erg (Table 1). The rough agreement among the results is not surprising given the very different methods used (with different assumptions) and the fact that the modeling of Prentice et al. (2018) is limited to optical spectra, and Yamanaka et al. (2017) only consider the optical/NIR emission of SN 2016coi during the early photospheric phase.

3. OPTICAL SPECTROSCOPY

3.1. Data Analysis

We obtained optical spectroscopy of SN 2016coi from a few days until $t > 400$ days post explosion with a variety of instruments on different telescopes (Table A7). The spectroscopic log can be found in Table A8. We extracted our time series of optical spectra with IRAF following standard procedures. Comparison lamps and standard stars acquired during the same night and with the same instrumental setting have been used for the wavelength and flux calibrations, respectively. When possible, we further removed telluric bands using standard stars.

Our spectroscopic campaign comprises 65 spectra (Fig. 4). The overall evolution of SN 2016coi is similar to that of type-Ic SNe. At early times $t \lesssim 60$ d the blue part of the spectrum at $\lambda \lesssim 5500$ Å is dominated by blends of several Fe II multiplets. We identify the main spectral feature at ~ 6000 Å as Si II $\lambda 6355$. Before maximum light, we associate the absorption feature around ~ 5500 Å to He I $\lambda 5876$, with possible contamination by Na I D. Na I dominates after maximum light. At $\lambda > 7000$ Å the spectra of SN 2016coi show

emission associated with O I $\lambda\lambda 7771, 7774, 7775$ and the Ca II NIR triplet. Nebular features start to appear ~ 90 d after explosion, when the forbidden [O I] $\lambda\lambda 6300, 6364$ and the [Ca II] $\lambda\lambda 7291, 7323$ doublets begin to emerge.

In Fig. 5 we show a zoomed-in plot of the nebular spectrum acquired with MMT+BlueChannel at ~ 400 d after explosion. We plot the region of the forbidden [O I] $\lambda\lambda 6300, 6364$, [Ca II] $\lambda\lambda 7291, 7323$ doublets, and semi-forbidden Mg I] $\lambda 4571$ emission line. We use gaussian profiles to model each emission line. For the doublets, we kept the separation between the two components fixed, while allowing for rigid shifts of the overall profile (this scheme will also be followed in §7.1). This simple approach allows us to adequately reproduce the emission line profiles (Fig. 5). We find that the ratio between the oxygen lines fluxes is ~ 2.6 , in reasonable agreement with the theoretical expectation of ~ 3 . However, the doublet is blue-shifted by ~ 10 Å (~ 400 km s $^{-1}$). We find similar blue-shifts for the Ca and Mg lines. Blue-shifted oxygen line profiles of this kind are not uncommon in type Ibc SN nebular spectra, and several causes have been invoked to explain this observed phenomenology, including dust obscuration, internal scattering, contamination from other lines or residual opacity in the core of the ejecta (Modjaz et al. 2008; Taubenberger et al. 2009; Milisavljevic et al. 2010). We do not observe asymmetric structures in the spectral lines, nor do we detect any sharp decrease in the light curve of SN 2016coi, therefore we can confidently exclude the presence of dust (Elmhamdi et al. 2003, 2004). As the [O I] forbidden doublet is fairly isolated, we disfavour contamination from other lines as the origin for the blue-shift. The fact that lines of different species show this behaviour might suggest a geometrical effect. An asymmetric explosion with a bulk of material moving towards the observer could indeed cause the blue-shift. Qualitative inferences on the geometry and distribution of the oxygen-rich ejecta in SN 2016coi can be drawn from the line profile of the forbidden [O I] $\lambda\lambda 6300, 6364$ (Modjaz et al. 2008; Taubenberger et al. 2009; Milisavljevic et al. 2010). Double-peaked oxygen lines are usually interpreted to be formed in asymmetric explosions viewed at a high angle between the observer point of view and the jet direction (Maeda et al. 2008; Taubenberger et al. 2009). As shown in Fig. 5, the oxygen doublet in SN 2016coi presents a single, symmetric profile, reproducible with simple Gaussian functions. This result is consistent with spherically symmetric ejecta. As Maeda et al. (2008) have shown that an asymmetric profile would not develop for asymmetric explosions viewed from angles below $\sim 50^\circ$, an asymmetric explosion cannot be ruled out. However, the asymmetric explosion scenario might actually be supported by the red excess visible in both the oxygen and magnesium line. Indeed, magnesium and oxygen are expected to have similar spatial distribution

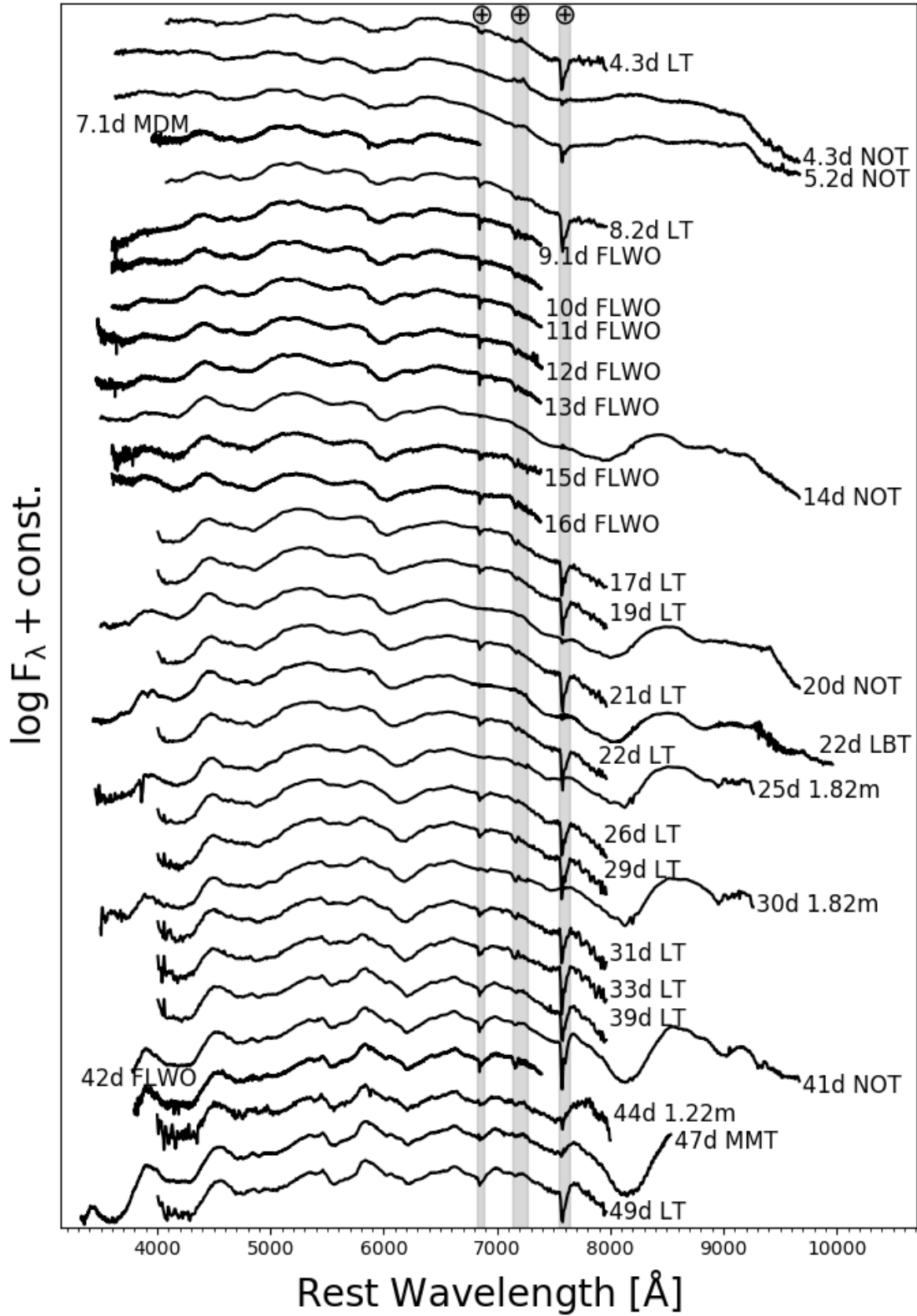


Figure 4. Optical spectral evolution of SN 2016coi. The spectra are presented in the rest-frame ($z = 0.003646$) and have been corrected for Galactic extinction along the line of sight. The spectra are shifted vertically for displaying purposes. Spectra are labeled based on the epoch of their acquisition and telescope used. The gray vertical bands mark the positions of the telluric O_2 A and B absorption bands.

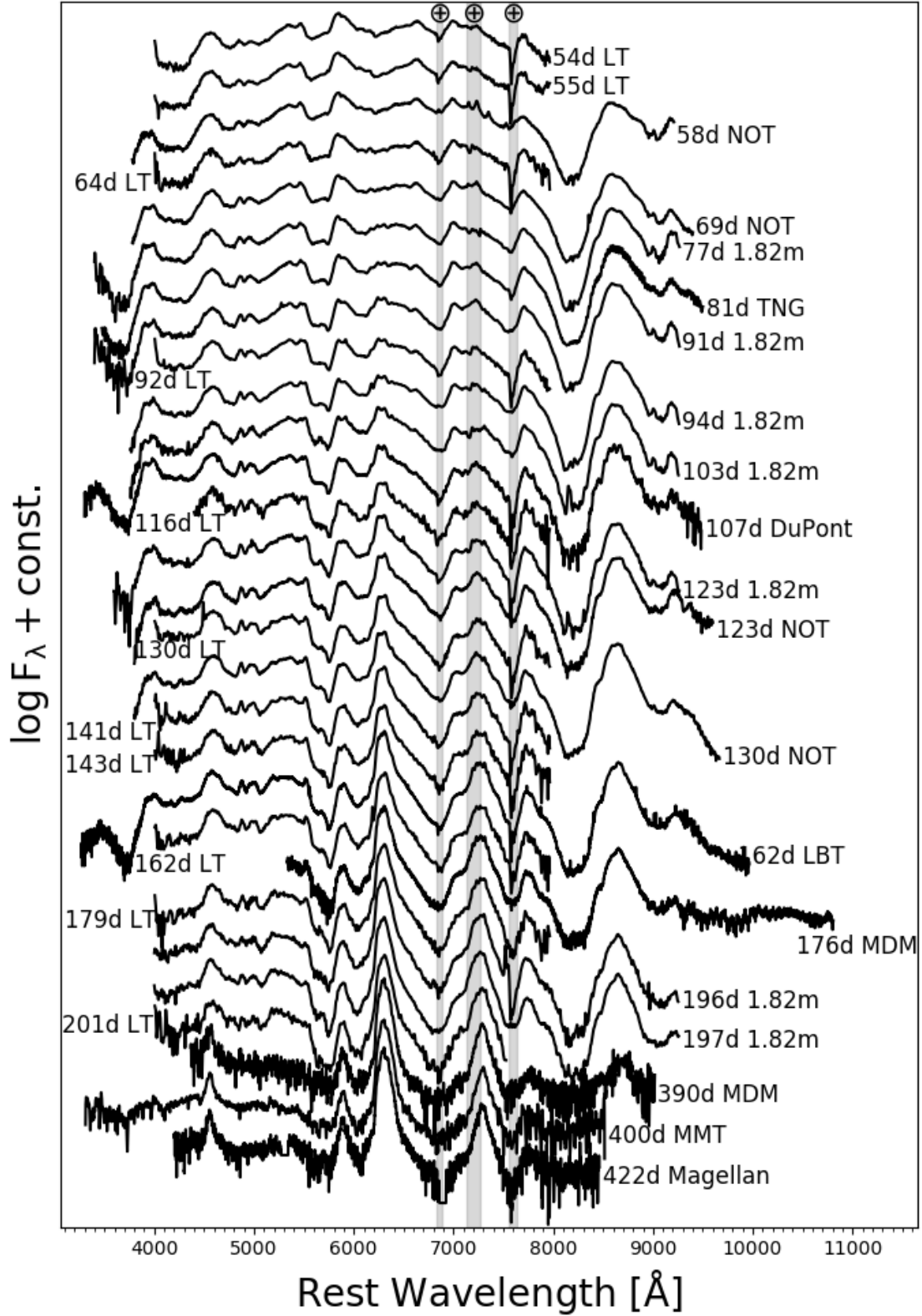


Figure 4. *Continued:* Optical spectral evolution of SN 2016coi. The spectra are presented in the rest-frame ($z = 0.003646$) and have been corrected for Galactic extinction along the line of sight. The spectra are shifted vertically for displaying purposes. Spectra are labeled based on the epoch of their acquisition and telescope used. The gray vertical bands mark the positions of the telluric O_2 A and B absorption bands.

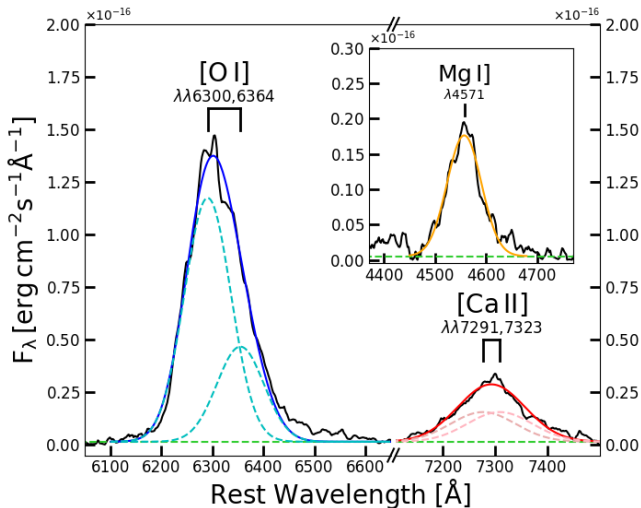


Figure 5. A zoomed-in plot of the spectral region of the [O I] $\lambda\lambda 6300, 6364$, [Ca II] $\lambda\lambda 7291, 7323$ and Mg I $\lambda 4571$ lines of the MMT+BlueChannel nebular spectrum acquired on 2017, June 28 (~ 400 d after explosion). Gaussian profiles have been used to reconstruct the doublet components of the emission features. The observed lack of asymmetry of the [O I] emission feature might result from spherically symmetric ejecta, or possibly from an axisymmetric explosion, viewed at an angle below 50° .

within the SN ejecta (e.g., Maeda et al. 2006; Taubenberger et al. 2009). Such an excess, visible in both features, is unlikely to be caused by line contamination, and is rather the result of ejecta asymmetries common to both line emission regions.

We conclude with a consideration on intrinsic reddening. In our highest resolution spectra acquired on November 2, 2016 UT (~ 162 days after first light) with LBT+MODS, we find a weak narrow Na I D absorption at the redshift of the host galaxy, from which we infer $E(B-V)_{\text{host}} \sim 0.017$ mag (Turatto et al. 2003; Poznanski et al. 2012). However, given the large uncertainties of this method (Phillips et al. 2013), and the lack of evidence for significant $E(B-V)_{\text{host}}$, in the following we assume $E(B-V)_{\text{host}} = 0$ mag.⁷ This assumption has no impact on our conclusions. Following Schlafly & Finkbeiner (2011), the Milky Way color excess in the direction of SN 2016coi is $E(B-V)_{\text{MW}} = 0.075$ mag, which we use to correct our spectro-photometric data for extinction.

3.2. SN Classification and presence of Helium in the ejecta

SN 2016coi initially showed spectral similarities to type Ic-BL SNe (and in particular to SN 2006aj, associated with GRB 060218) but later evolved to resemble a normal type Ic SN (Fig. 4). Indeed, both Kumar et al. (2018) and Prentice

et al. (2018) identified SN 2016coi as being an intermediate object between the two classes, while Yamanaka et al. (2017) classified SN 2016coi as a BL-Ib SN, because of the presence of helium in the spectra and expansion velocities larger than in normal type Ib SNe. We quantitatively explore the questions of how the ejecta velocity of SN 2016coi compares to other H-stripped SNe, and the presence of He in its ejecta below.

We compare SN 2016coi to the spectral templates of normal type Ic SNe and BL-Ic SNe from Modjaz et al. (2016) in Fig. 6 after applying the same renormalization procedure. The result is presented for three different epochs: 10 days before maximum light, around maximum light, and 20 days after maximum light. Fig. 6 demonstrates that the typically prominent Ca II H+K absorption feature of type Ic SNe spectra is almost absent in SN 2016coi (Fig. 6, top and middle panels), in closer similarity to type Ic-BL SN spectra. Notably, SN 2016coi shows a prominent absorption feature at ~ 6000 Å that we identify as Si II with $v \sim 19000$ km s⁻¹, which is typically not present with this strength in normal type Ic SNe (e.g., Parrent et al. 2016).

From our comparison, SN 2016coi more closely resembles normal type Ic SNe, especially before maximum light. Compared to type Ic-BL SNe, SN 2016coi shows more prominent peaks and troughs (upper panels in Fig. 6), as a result of its lower ejecta velocities before maximum light, which cause less severe blending of the spectral features. Compared to normal type Ic SNe, however, SN 2016coi shows systematically blue-shifted spectral features. Modjaz et al. (2016) showed that in type Ic SNe (both normal and broad-line) the “broadness” of the spectral features correlates with the blue-shift of their minima, as is expected from an expanding atmosphere (e.g., Dessart et al. 2011). However, with very blue-shifted absorption minima similar to type Ic-BL, but less prominent broadening, SN 2016coi seems to deviate from this trend.

Modjaz et al. (2016) used the Fe II $\lambda 5169$ to show this correlation between the blue-shift of the minima and the broadening of the absorption feature. We use the same fitting technique as in Modjaz et al. (2016) to measure the broadening of this same line for SN 2016coi at maximum light, obtaining $v_{\text{broad}} \sim 2380$ km s⁻¹. Comparing this value with their Fig. 7, it is possible to see how this is quite low for a BL-Ic, while the velocity inferred from the position of the minimum of the line profile is $v_{\text{min}} \sim 18050$ km s⁻¹, well within the range of the other BL-Ic of their sample. Another event that had very blue-shifted minima but relatively low broadening was PTF 12gzk (Ben-Ami et al. 2012). These observations were interpreted as resulting from either the departure from spherical symmetry, or from a steep gradient of the density profile of the progenitor envelope. Interestingly, Ben-Ami et al. (2012) inferred a massive ejecta of $25\text{--}35M_{\odot}$ and a

⁷ This is in agreement with the assumption by Yamanaka et al. (2017) and Kumar et al. (2018). On the other hand, Prentice et al. (2018) assumed a host extinction of $E(B-V)_{\text{host}} = 0.125$ mag.

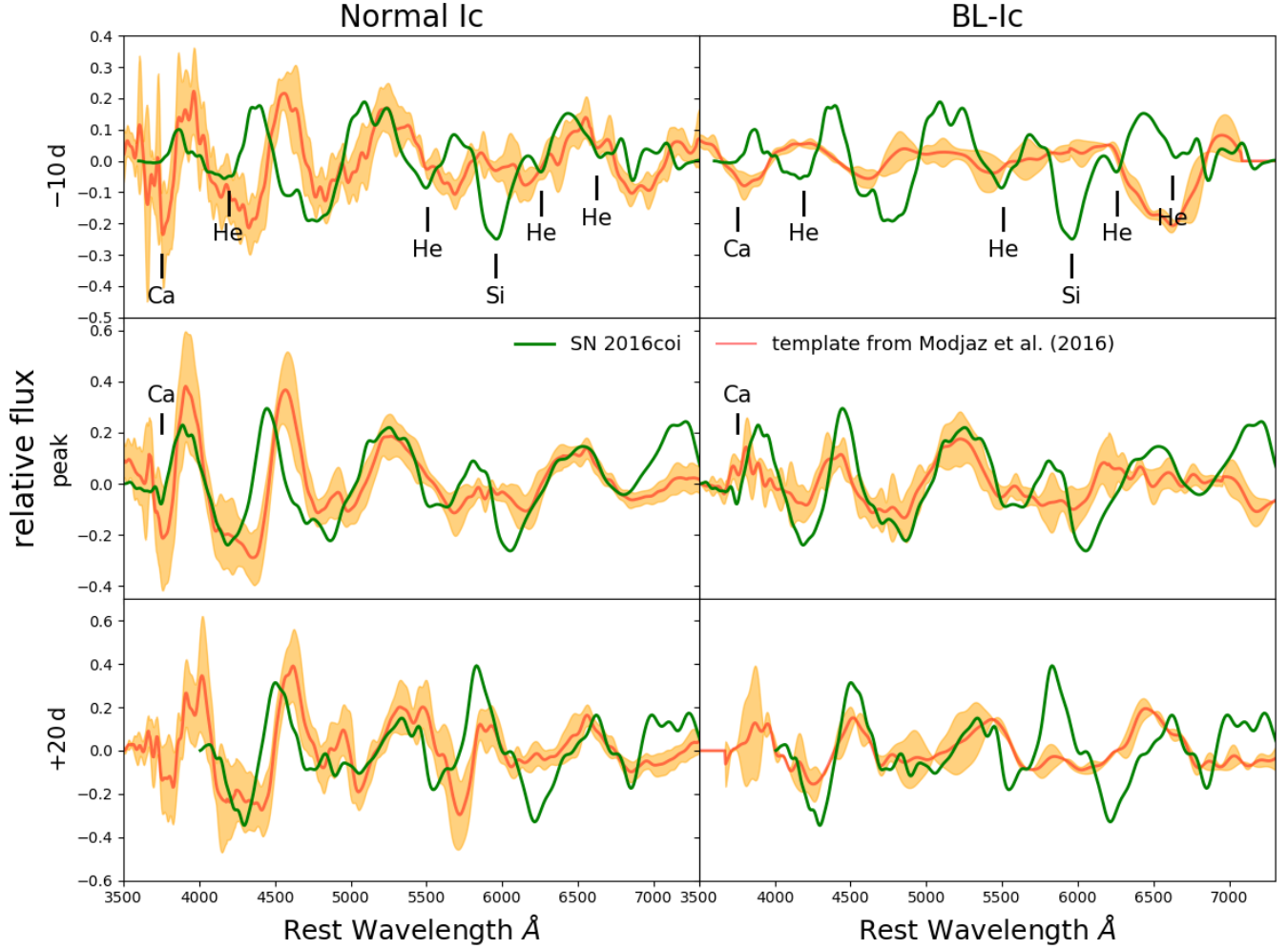


Figure 6. Comparison between the spectra of SN 2016coi with the spectral templates from Modjaz et al. (2016) at -10 d from peak, maximum light and $+20$ d after peak (top, middle and bottom panels, respectively). We compare SN 2016coi to normal type Ic-SNe (left panels) and with Ic-SNe with broad lines (i.e., type BL-Ic; right panels). The orange shaded region represents a 1σ standard deviation from the mean. SN 2016coi shares similarities with both classes, and it can be considered as an intermediate case that bridges the gap between type Ic and BL-Ic SNe.

large kinetic energy of $5-10 \times 10^{51}$ erg for PTF 12gzk, which is comparable to SN 2016coi. SN 2016coi thus shows spectral properties that are intermediate between type Ic-BL SNe (with which SN 2016coi also shares the large kinetic energy $E_k > 10^{51}$ erg but lower velocities before peak) and normal type Ic SNe. These results agree with the findings by Kumar et al. (2018) and Prentice et al. (2018).

We next address the presence of He in the ejecta of SN 2016coi (in Fig. 6 we marked the position of the He I $\lambda 4472$, $\lambda 5876$, $\lambda 6678$ and $\lambda 7065$ lines). We investigate the velocity evolution of the most prominent spectral features among those associated with He I at 5876 Å in Fig. 7, and use the velocity evolution inferred from Si II $\lambda 6355$ as a comparison. From Fig. 7 we find that He and Si show a very similar temporal evolution, with expansion velocities evolving from $v \sim 20000 \text{ km s}^{-1}$ at ~ 2 weeks before maximum

light, to $v \sim 15000 \text{ km s}^{-1}$ around peak. The identification of He might inspire a connection with type Ib SNe. However, we note that in SN 2016coi the He features slowly subside (by the time of maximum light He absorption is no longer prominent, Fig. 7), while in type Ib SNe He features develop with time (e.g., Filippenko 1997; Gal-Yam 2017). The presence of He in SN 2016coi has been recognized as a peculiar characteristic of SN 2016coi by Yamanaka et al. (2017), Kumar et al. (2018) and Prentice et al. (2018). Yamanaka et al. (2017) concluded the presence of He in SN 2016coi based on the comparison with a smoothed out and blueshifted version of the type Ib SN 2012au (Takaki et al. 2013), finding a correspondence with the position of the main helium features. They also cross-checked this result with synthetic spectra generated with the code SYN++ (Thomas et al. 2011). Kumar et al. (2018) adopted a similar strategy to the one pre-

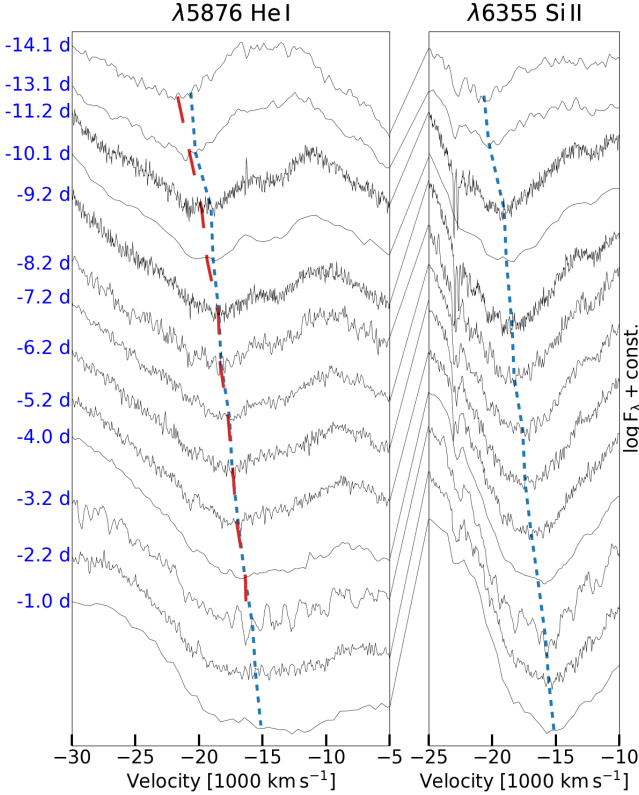


Figure 7. *Right panel:* Evolution of the Si II $\lambda 6355$ line before maximum light in the velocity space. The position of the minimum of the absorption feature is marked with a vertical blue short-dashed line. *Left panel:* Evolution of the 5500 Å feature, assumed to be the He I $\lambda 5876$ line. The position of the minimum of the absorption feature is marked with a red long-dashed line. The velocity of the absorption minimum of Si II $\lambda 6355$ is also shown for comparison with a blue short dashed line. The match between the evolution of the two lines suggest a correct interpretation of the 5500 Å feature as the He I $\lambda 5876$ line. By the time of maximum light, He absorption is no longer apparent in the spectra of SN 2016coi, and the presence of He becomes hard to quantify due the possible emergence of the Na I $\lambda\lambda 5890, 5896$ doublet.

sented in this work, performing a detailed velocity analysis of the single features. With their 1D Monte Carlo spectra synthesis code, Prentice et al. (2018) investigated what other elements could be responsible for the absorption at ~ 5500 Å. They showed that He is indeed the favored interpretation, and that in the absence of He, unphysical amounts of Al II and Na I would be necessary to reproduce the observed spectra.

Similar velocities between Si-rich and He-rich ejecta indicates a clear departure from the expectations of a homologous explosion of a stratified progenitor star where the outer He-rich layers are expected to expand significantly faster than the inner Si-rich layers of ejecta. This finding suggests a higher level of mixing of the ejecta, which might be con-

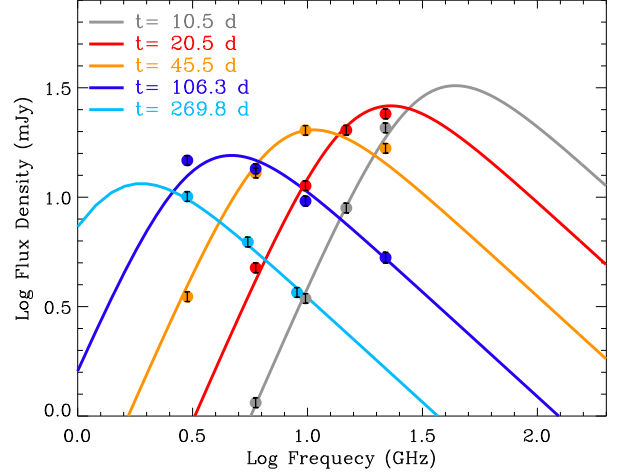


Figure 8. Radio SED of SN 2016coi at 10.5, 20.5, 45.5, 106.3 and 269.8 days after first light (see Table A9). The radio emission from SN 2016coi is well described by a synchrotron self-absorbed spectrum (SSA) with spectral peak frequency $\nu_{pk} \propto t^{-0.97 \pm 0.02}$ and peak flux $F_{pk} \propto t^{-0.31 \pm 0.02}$. We find $F_\nu \propto \nu^{2.4 \pm 0.1}$ for the optically thick part of the spectrum, consistent with $F_\nu \propto \nu^{5/2}$ as expected for SSA. The optically thin part of the spectrum $F_\nu \propto \nu^{-(p-1)/2}$ scales as $F_\nu \propto \nu^{-0.96 \pm 0.05}$, from which we infer $p \sim 3$, as typically found in radio SNe (e.g., Chevalier & Fransson 2006).

nected with the capability to excite He (and hence the detection of He in our spectra).

4. RADIO

4.1. VLA Data Analysis

We present in Fig. 8 multi-band observations of SN 2016coi taken up to 278 days post explosion with the Karl G. Jansky Very Large Array (VLA, projects 16A-447 and 17A-167). The details of these data are given in Table A9. We used standard phase referencing mode and the standard flux density calibrators 3C48 and 3C286 were used to set the absolute flux density scale. The data were calibrated using the VLA pipeline in CASA version 5.4.1, and imaged in CASA (McMullin et al. 2007) following standard routines. We used Briggs weighting with a robust parameter of one to image. In the epochs where SN 2016coi was sufficiently bright, we performed phase-only self-calibration on the target. We subsequently fitted the sources in the image plane using the Python Blob Detector and Source Finder (PyBDSF, Mohan & Rafferty 2015). The uncertainties listed in Table A9 take into consideration the errors on the fit and a 5% uncertainty on the absolute flux density scale. The flux density evolution of SN 2016coi at ~ 8.5 GHz is presented in Fig. 9 (left panel), together with a comparison with other SESNe and GRBs at the same frequency.

4.2. Inferences on the Progenitor Properties and Mass-loss History from Radio Observations

Radio emission in type Ibc SNe is well explained as synchrotron emission from relativistic electrons with a power-law distribution of Lorentz factors γ ($N_e(\gamma) \propto \gamma^{-p}$) that gyrate in shock amplified magnetic fields (e.g., [Chevalier & Fransson 2006](#)). SN 2016coi shows the characteristic “bell-shaped” spectrum of radio sources dominated by synchrotron self-absorption (SSA), with spectral peak flux $F_{pk} \propto t^{-0.31 \pm 0.02}$ and peak frequency $\nu_{pk} \propto t^{-0.97 \pm 0.02}$. By fitting a broken power-law to the radio data of SN 2016coi we find that the optically thin part of the spectrum $F_\nu \propto \nu^{-(p-1)/2}$ scales as $F_\nu \propto \nu^{-0.96 \pm 0.05}$, which implies $p \sim 3$, as typically found in radio SNe (e.g., [Chevalier & Fransson 2006](#)). For the optically thick part of the spectrum our fits indicate $F_\nu \propto \nu^{2.4 \pm 0.1}$, consistent with the SSA expectation $F_\nu \propto \nu^{5/2}$. We find no evidence for free-free external absorption (e.g., [Weiler et al. 2002](#)), which would cause the optically thick spectrum to be steeper than $F_\nu \propto \nu^{5/2}$.

Using the SSA formalism by [Chevalier \(1998\)](#), the best fitting $F_{pk}(t)$ and $\nu_{pk}(t)$ above translate into a constrain on the outer shock radius evolution $R_{sh}(t)$, magnetic field $B(R)$ and circumstellar density profile $\rho_{CMS}(R)$. We find evidence for a slightly decelerating blastwave with $R_{sh}(t) \propto t^{0.82 \pm 0.02}$ and $B(R) \propto R^{-1.14 \pm 0.03}$ propagating into a medium with density profile $\rho_{CSM}(R) \propto R^{-1.84 \pm 0.04}$. The inferred $B(R)$ profile is steeper than the $B(R) \propto R^{-1}$ scaling typically observed in H-stripped SNe (e.g., [Horesh et al. 2013](#)) and causes the observed decay of $F_{pk}(t)$ with time. Normal non-decelerating type Ibc SNe typically show a constant $F_{pk}(t)$ ([Chevalier 1998](#)). The inferred $\rho_{CSM}(R) \propto R^{-1.84 \pm 0.04}$ is slightly flatter than a pure wind density profile $\rho_{wind} \propto R^{-2}$, which implies an *increasing* effective mass-loss with radius $\dot{M}_{eff} \propto R^2 \rho_{CSM} \propto R^{0.16 \pm 0.04}$. We find $\dot{M}_{eff}(R_2) \sim 2 \times \dot{M}_{eff}(R_1)$, where $R_1 \sim 4 \times 10^{16}$ cm is the blast wave radius at 10.5 days and $R_2 \sim 10^{17}$ cm is the blast wave radius at the end of the radio monitoring presented here, at $\delta t \sim 280$ days. For an assumed wind velocity $v_w = 1000 \text{ km s}^{-1}$ (appropriate for compact massive stars like WRs; [Crowther 2007](#)), these results imply that the stellar progenitor of SN 2016coi experienced a phase of enhanced mass-loss ≥ 30 yrs before collapse. We estimate that ~ 30 yrs before death, the stellar progenitor of SN 2016coi was losing twice the amount of material per unit time compared to ~ 10 yrs before stellar demise.

According to the self-similar solutions by [Chevalier \(1982\)](#) the interaction of a steep SN outer ejecta profile $\rho_{SN} \propto R^{-n}$ with a shallower medium with $\rho_{CSM} \propto R^{-s}$ produces an interaction region that expands as $R_{sh} \propto t^m$ with $m = (n-3)/(n-s)$. For SN 2016coi, the inferred $R_{sh}(t) \propto t^{0.82 \pm 0.02}$ and $s = -1.84 \pm 0.04$ thus imply $n = 8.2 \pm 0.7$. This result is consistent with the theoretical calculations of the post-explosion outer-ejecta density profiles of compact stars (e.g., WRs), for which [Matzner & McKee \(1999\)](#) find $n \sim 10$. Extended red supergiants can have steeper outer density gradients (e.g.

$\gtrsim 20$; [Fransson et al. 1996](#)). We conclude that radio observations of SN 2016coi favor a compact progenitor star at the time of collapse.

All the considerations above do not depend on the assumed shock microphysical parameters ϵ_B and ϵ_e (i.e., the fraction of post-shock energy in magnetic fields and electrons, respectively). Below we provide the best-fitting values of the shock radius R_{sh} , internal energy U , magnetic field B and effective mass loss \dot{M}_{eff} at a given reference epoch under the assumption of equipartition of energy between electrons, protons and B (i.e., $\epsilon_B = \epsilon_e = 0.33$). Following [Chevalier \(1998\)](#), we find:

$$B(10.5 \text{ d}) = (4.0 \pm 0.2) \left(\frac{\epsilon_e}{0.33} \right)^{-4/19} \left(\frac{\epsilon_B}{0.33} \right)^{+4/19} \text{ G}, \quad (1)$$

$$R_{sh}(10.5 \text{ d}) = (3.1 \pm 0.1) \times 10^{15} \left(\frac{\epsilon_e}{0.33} \right)^{-1/19} \left(\frac{\epsilon_B}{0.33} \right)^{+1/19} \text{ cm}. \quad (2)$$

The outer shock radius of Eq. 2 does not strongly depend on the assumed microphysical parameter values. From Eq. 2, we can thus derive a solid estimate of the average SN shock velocity at $t = 10.5$ days $v_{sh} \sim 0.15c$. This value is similar to normal type Ibc SNe (e.g., [Chevalier & Fransson 2006](#)) and different from GRB-SNe and relativistic SNe, which show evidence for ultra-relativistic and mildly relativistic outflows ([Soderberg et al. 2010b](#); [Margutti et al. 2014](#); [Chakraborti et al. 2015](#)). The effective mass-loss is:

$$\dot{M}_{eff}(10.5 \text{ d}) = (3.6 \pm 0.3) \times 10^{-5} \left(\frac{\epsilon_e}{0.33} \right)^{-8/19} \left(\frac{\epsilon_B}{0.33} \right)^{-11/19} \text{ M}_\odot \text{ yr}^{-1}, \quad (3)$$

and the shock internal energy is:

$$U(10.5 \text{ d}) = (1.1 \pm 0.1) \times 10^{47} \left(\frac{\epsilon_e}{0.33} \right)^{-11/19} \left(\frac{\epsilon_B}{0.33} \right)^{-8/19} \text{ erg}. \quad (4)$$

Under the assumption of equipartition, the internal energy value $U(10.5 \text{ d}) = (1.1 \pm 0.1) \times 10^{47}$ erg sets a lower limit on the true internal energy of the system at $t = 10.5$ d, and on the kinetic energy of the radio emitting material. U increases with time, as the shock decelerates and more kinetic energy of the shock wave is converted into internal energy. At $t \sim 280$ d we measure $v_{sh} \sim 0.06 \pm 0.01 c$ and $U(280 \text{ d}) = (7.6 \pm 0.9) \times 10^{47}$ erg (in equipartition), which places SN 2016coi among energetic shocks from normal H-stripped SNe (Fig. 2 in [Margutti et al. 2014](#)).

Realistic values of ϵ_e and ϵ_B in SN shocks are likely < 0.33 , implying that both the equipartition \dot{M}_{eff} and U are lower limits on the true values of the system. For comparison, for more realistic values of $\epsilon_e = 0.1$ and $\epsilon_B = 0.01$ (typical values for relativistic shocks; [Sironi & Spitkovsky 2011](#)), we infer $\dot{M}_{eff}(10.5 \text{ d}) = (4.5 \pm 0.4) \times 10^{-4} \text{ M}_\odot \text{ yr}^{-1}$ and $U(280 \text{ d}) = (6.7 \pm 0.8) \times 10^{48}$ erg. Recent kinetic simulations of trans-relativistic shocks suggest values of $\epsilon_B \sim 0.01$

and $\epsilon_e \gtrsim 10^{-3}$ (Park et al. 2015; Crumley et al. 2019). An $\epsilon_e \sim 3 \times 10^{-3}$ would imply a very energetic explosion, with $U(280\text{d}) = (5.1 \pm 0.6) \times 10^{49}$ erg, however it also yields an unrealistic $\dot{M}_{eff}(10.5\text{d}) = (2.0 \pm 0.2) \times 10^{-3} M_\odot \text{yr}^{-1}$. Similar values of mass-loss are more typical of progenitor stars of Type IIa SNe and are likely too high for SN 2016coi. In general, the theory of particle acceleration at strong trans-relativistic shocks not only does not explain large values of ϵ_e , but also does not produce the typical $p \sim 3$ often inferred in radio SNe. The explanation of Chevalier & Fransson 2006 invokes shocks modified by the dynamical backreaction of the accelerated particles, which was thought to lead to concave spectra, steeper than E^{-2} below a few GeV, but such an argument is at odds with observations of Galactic SN remnants (Caprioli 2012).

A robust upper limit on the effective mass-loss can be inferred from the lack of free-free external absorption in the radio spectra. Indeed, the absence of a low-frequency cut-off can be used to constrain the environment density independently from the shock microphysics. From Weiler et al. (2002), the free-free optical depth of unshocked ionized gas in a wind density profile is:

$$\tau_{\text{ff}} \simeq \frac{\alpha_{\text{ff}r}}{3} \approx 10 \left(\frac{\nu}{10\text{GHz}} \right)^{-2} \left(\frac{T_g}{10^4\text{K}} \right)^{-3/2} \dot{M}_{-3}^2 \left(\frac{v_{sh}}{0.1c} \right)^{-3} t_{\text{wk}}^{-3}, \quad (5)$$

where \dot{M} is in units of $10^{-3} M_\odot \text{yr}^{-1}$ for $v_w = 1000 \text{ km s}^{-1}$, T_g is the temperature of the gas, normalized to a value $T_g \gtrsim 10^4$ K typical of photoionized gas, and time is units of 1 week. Furthermore, we used $\kappa_{\text{es}} = 0.38 \text{ cm}^2 \text{ g}^{-1}$ for fully ionized solar-composition ejecta and $\alpha_{\text{ff}} \approx 0.03 n_w^2 \nu^{-2} T_g^{-3/2} \text{ cm}^{-1}$ as the free-free absorption coefficient. The lack of evidence for free-free absorption at 10.5 days at $\nu = 5.9$ GHz, and at 45.5 days at $\nu = 3$ GHz demands $\tau_{\text{ff}} \ll 1$, which translates into $\dot{M} < 10^{-3} M_\odot \text{yr}^{-1}$ for $v_w = 1000 \text{ km s}^{-1}$.

5. X-RAYS

5.1. *Swift*-XRT and XMM-Newton Data Analysis

The X-Ray Telescope (XRT; Burrows et al. 2005), on board the Neil Gehrels *Swift* Observatory, started observing SN 2016coi on May 27, 2016 ($\delta t \sim 2$ days post explosion) until April 17, 2017 ($\delta t \sim 326$ days), for a total exposure time of 94.4 ks. *Swift*-XRT data have been analyzed using the latest HEASoft release v6.22 and corresponding calibration files. Standard filtering and screening criteria have been applied (see Margutti et al. 2013 for details). An X-ray source is clearly detected at the location of SN 2016coi until $\delta t \sim 100$ days post explosion. The X-ray source is located $\sim 30''$ from the host galaxy nucleus (which is not detected by *Swift*-XRT and does not represent a source of contaminating X-ray emission; see Fig. 1, bottom panel) and shows a fading behavior with time, from which we conclude

that the detected X-ray emission is physically associated with SN 2016coi. The spectrum can be fit with an absorbed power-law spectral model with best fitting photon index $\Gamma = 1.78 \pm 0.18$. We find no evidence for intrinsic absorption and we place a 3σ limit for the neutral hydrogen absorption column $NH_i < 0.4 \times 10^{22} \text{ cm}^{-2}$. The Galactic NH_i in the direction of SN 2016coi is $NH_{mw} = 0.056 \times 10^{22} \text{ cm}^{-2}$ (Kalberla et al. 2005). For this spectrum, the 0.3-10 keV count-to-flux conversion factor is $\sim 4.22 \times 10^{-11} \text{ erg s}^{-1} \text{ cm}^{-2} \text{ ct}^{-1}$ (unabsorbed). The *Swift*-XRT count-rate and flux-calibrated light-curve is reported in Table A10 and shown in Fig. 9 (right panel).

We started deep X-ray observations of the field of SN 2016coi with XMM-Newton on June 6, 2016 (PI Margutti). We obtained two epochs of observations at $\delta t \sim 11.5$ days (exposure time of 29 ks, observation ID 0782420201) and $\delta t \sim 27.5$ days (exposure of 28 ks, observation ID 0782420301). XMM data have been analyzed with SAS (v15.0). The first observation was heavily affected by proton flaring and the net exposure time of the EPIC-pn camera after filtering out the intervals of high background was reduced to 1.1 ks, whereas for the second epoch we have 13.4 ks net exposure time. SN 2016coi is clearly detected by all three cameras in both epochs. The inferred EPIC-pn count-rate is $(4.0 \pm 0.7) \times 10^{-2} \text{ cts}^{-1}$ and $(1.7 \pm 0.2) \times 10^{-2} \text{ cts}^{-1}$ (0.3-10 keV) for the first and second epoch, respectively. A spectrum extracted from the first (second) epoch can be fitted with an absorbed power-law model with $\Gamma = 1.9 \pm 0.3$ ($\Gamma = 1.8 \pm 0.3$). The corresponding flux is $\sim 1.1 \times 10^{-13} \text{ erg s}^{-1} \text{ cm}^{-2}$ and $\sim 0.6 \times 10^{-13} \text{ erg s}^{-1} \text{ cm}^{-2}$ for the first and the second epoch, respectively, consistent with the results from our *Swift*-XRT monitoring (Table A10 and Fig. 9).

We do not find evidence for significant spectral evolution. From a joint fit of *Swift*-XRT and XMM data we find a best-fitting $\Gamma = 1.80 \pm 0.10$ and $NH_i < 0.17 \times 10^{22} \text{ cm}^{-2}$.

5.2. Inferences on the Mass-loss History of the Stellar Progenitor from X-ray Observations

In normal H-poor SNe, the early time ($\delta t \lesssim 30$ days) X-ray emission is expected to be dominated by Inverse Compton (IC) scattering of optical photospheric photons by relativistic electrons accelerated at the shock fronts (e.g., Björnsson & Fransson 2004; Chevalier & Fransson 2006). The non-thermal X-ray spectrum of SN 2016coi with $\Gamma \sim 2$ and lacking evidence for intrinsic absorption is consistent with this expectation. Adopting the formalism by Margutti et al. (2012), the IC emission depends on: (i) density profile of the SN ejecta ρ_{ej} ; (ii) properties of the electron distribution responsible for the up-scattering $N_e(\gamma)$; (iii) blastwave velocity, which, in turns, depends on the circumstellar medium (CSM) density and explosion's parameters (kinetic energy

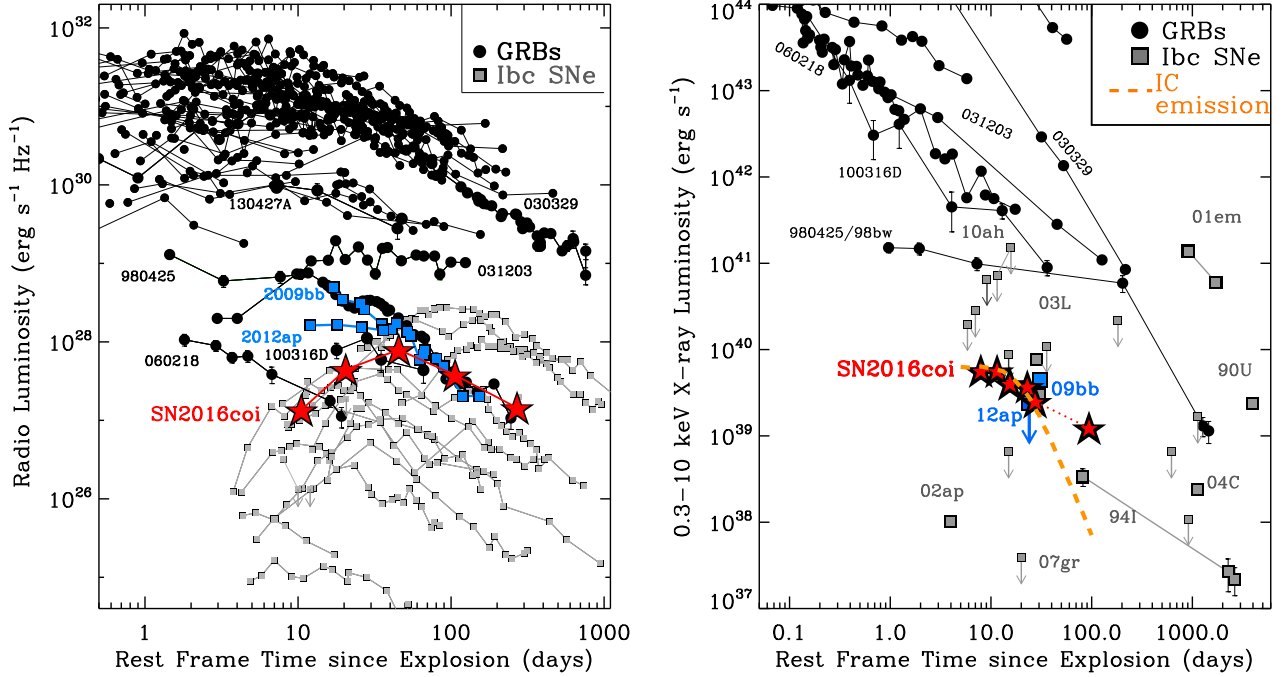


Figure 9. Radio ~ 8.5 GHz (left panel) and X-ray (right panel) emission from SN 2016coi (red stars) in the context of normal H-stripped SNe (grey squares), relativistic SNe (blue squares) and GRBs (black filled circles). While being significantly fainter than GRB-SNe, SN 2016coi competes in X-ray luminosity with relativistic SNe and it is significantly more luminous than the BL-Ic SN 2002ap. The radiation from SN 2016coi is well explained by synchrotron emission at radio wavelengths at all times, while the X-rays are dominated by Inverse Compton (IC) emission (dashed orange line). At late times the IC scattering model underestimates the observed X-ray flux of SN 2016coi, suggesting additional contributions from other mechanisms. References: Immler et al. (2002); Pooley & Lewin (2004); Soria et al. (2004); Soderberg et al. (2005); Perna et al. (2008); Soderberg et al. (2010b); Chakraborti et al. (2011); Chandra & Frail (2012); Horesh et al. (2013); Margutti et al. (2013); Chakraborti et al. (2014); Corsi et al. (2014); Margutti et al. (2014).

E_k and ejecta mass M_{ej}); (iv) optical bolometric luminosity of the SN (from §2.2), which is the ultimate source of photons that are upscattered to X-ray energies $L_{X,IC} \propto L_{bol}$. We parametrize the CSM density as a wind medium $\rho_{CSM} = \dot{M}/4\pi v_w R^2$ (where v_w is the progenitor wind and \dot{M} is the mass-loss rate) and we use $\rho_{ej} \propto R^{-n}$ with $n \sim 10$, as appropriate for SNe with compact progenitors (e.g., Matzner & McKee 1999; Chevalier & Li 2000), consistently with the results from the modeling of radio data in §4.2. We further assume a power-law distribution of electrons $N_e(\gamma) \propto \gamma^{-p}$ with $p \sim 3$ and $\epsilon_e = 0.1$ for consistency with the modeling of other SNe (e.g., Chevalier & Fransson 2006).

Considering the range of explosion parameters of §2.2 and assuming a wind velocity of $v_w = 1000 \text{ km s}^{-1}$, for a shock velocity of $v_{sh} \sim 0.1 c$ (§4.2) we infer a mass-loss rate of $\dot{M} \sim (1-2) \times 10^{-4} M_{\odot} \text{ yr}^{-1}$. Our X-ray analysis thus provides independent evidence that SN 2016coi exploded in a dense environment when compared to type Ic-BL SNe (Fig. 10). This suggests that the stellar progenitor of SN 2016coi experienced significant mass loss in the last years before core-collapse. This result is independent of ϵ_B . A comparison to Eq. 3 suggests that for $\epsilon_e = 0.1$ $\epsilon_B \leq 0.1$.

The right panel of Fig. 9 clearly shows that IC (dashed orange line) fails to reproduce the bright X-ray emission at ~ 100 days by a large factor. At these times, synchrotron emission is expected to dominate (e.g., Chevalier & Fransson 2006). The extrapolation of the optically thin $F_{\nu} \propto \nu^{-0.96}$ radio spectrum to the X-ray band under-predicts the observed X-ray emission by a large factor ~ 30 . The discrepancy between the extrapolation of synchrotron spectrum that best fits the radio and the observed X-ray data is even larger when we consider that the synchrotron cooling frequency $\nu_c = 18\pi m_e c q / (t^2 B^3 \sigma_T^2)$ is $\nu_c \sim 10^{11} - 10^{12} \text{ Hz}$ at ~ 100 days using B from Eq. 1 and $\epsilon_B = 0.01 - 0.1$ (where q is the electron charge and m_e is the electron mass). Above ν_c the flux density steepens as $F_{\nu} \propto \nu^{-p/2}$, leading to an even lower expected X-ray flux. The conclusion is that the late time $t \geq 100$ days X-ray emission from SN 2016coi is too luminous to be explained within the standard framework of synchrotron radiation from a population of electrons accelerated into a simple power-law distribution $N_e(\gamma) \propto \gamma^{-p}$.

The problem of having very luminous X-ray emission from H-stripped core-collapse SNe at late times is not new and was explored in detail by Chevalier & Fransson (2006). These authors favor an interpretation where the particle spectrum is

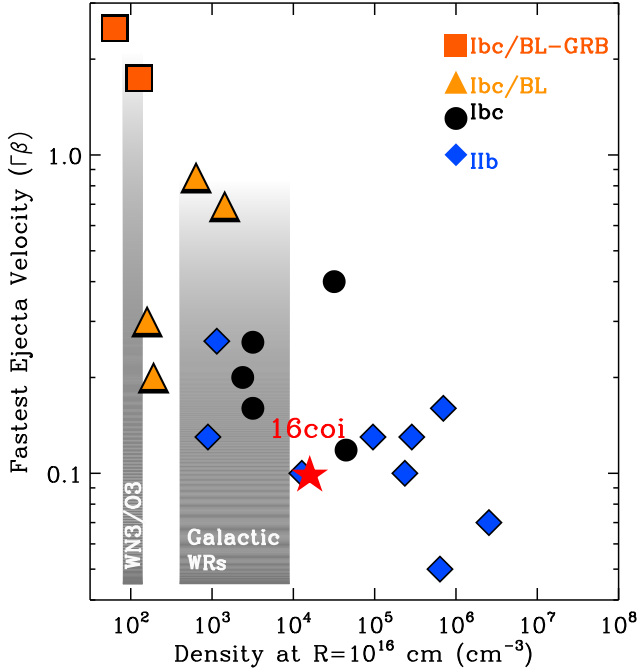


Figure 10. Fastest ejecta velocity in the explosion vs. environmental number density of SN 2016coi in the context of H-stripped core-collapse SNe. Type IIb SNe (blue diamonds) explode in the densest environments, while SN that accompany GRBs are associated with the lowest density environments (orange squares). Normal type Ibc SN are shown with black filled circles. SN with broad features in their spectra (Ibc/BL in the plot, orange triangles) also tend to be associated with low density media. An exception to this behavior is SN 2016coi, which exploded in a dense environment (red star). For SN 2016coi we show here the equipartition number density. The true number density in the environment of SN 2016coi is ~ 10 times the equipartition value if $\epsilon_B = 0.01$. Grey shaded regions: density in the environments of WRs and the recently discovered new type of WR stars WN3/O3 (de Jager et al. 1988; Marshall et al. 2004; van Loon et al. 2005; Crowther 2007; Massey et al. 2015). References: van Dyk et al. (1994); Fransson & Björnsson (1998); Berger et al. (2002); Weiler et al. (2002); Ryder et al. (2004); Soderberg et al. (2005); Chevalier & Fransson (2006); Soderberg et al. (2006b,a, 2008); Roming et al. (2009); Soderberg et al. (2010b,a); Krauss et al. (2012); Milisavljevic et al. (2013); Margutti et al. (2014); Kamble et al. (2014); Corsi et al. (2014); Chakraborti et al. (2015); Drout et al. (2016); Kamble et al. (2016); Margutti et al. (2017).

modified and becomes flatter for $\gamma \geq 1000$. The net effect is an increase of the X-ray synchrotron emission, while the effect on the radio synchrotron emission is minor (see their Fig. 1). At the time of writing it is unclear what physical effect might produce this shape of the particle spectrum, as the cosmic-ray dominated shocks invoked by Chevalier & Fransson (2006) have not been confirmed by recent particle-in-cell (PIC) simulations (Park et al. 2015). We end by noting that at the large mass-loss rates inferred for SN 2016coi in the case of deviation from equipartition $\dot{M}_{eff} \sim 5 \times 10^{-4} M_{\odot} \text{yr}^{-1}$,

the X-rays are likely to receive a contribution from free-free emission. From Chevalier & Fransson (2006), their Eq. 30, for this mass-loss rate we estimate $L_{x,ff} \sim 5 \times 10^{38} \text{erg s}^{-1}$ at $t \sim 100$ days, which is a factor ~ 2 lower than the observed X-ray emission at this epoch.

6. SEARCH FOR SHOCK BREAKOUT EMISSION AT HIGH ENERGIES

For compact massive H-stripped stars that are progenitors of (some) type Ibc SNe, the very first electromagnetic signal able to escape from the explosion site and reach the observer (i.e., the breakout pulse) is expected to peak at X-ray and γ -ray energies (e.g., SN 2008D; Soderberg et al. 2008). We searched for a high-energy pulse associated with the shock breakout of SN 2016coi using data collected by the InterPlanetary Network (IPN), which includes Mars Odyssey, Konus-Wind, RHESSI, INTEGRAL (SPI-ACS; Spectrometer on INTEGRAL-Anti-Coincidence System), *Swift*-BAT (Burst Alert Telescope) and *Fermi*-GBM (Gamma-Ray Burst Monitor). The IPN observes the entire sky with temporal duty cycle $\sim 100\%$ when all the experiments are considered. A total of 6 bursts were detected by the spacecraft of the IPN between May 22.4, 2016 and May 25.6, 2016, which covers the most likely explosion date window $\text{May } 23.9 \pm 1.5$ days that we inferred in §2.2. None has a localization region consistent with the position of SN 2016coi. We thus conclude that there is no evidence for a SN-associated shock breakout pulse down to the IPN sensitivity threshold with fluence $F_{\gamma} \sim 6 \times 10^{-7} \text{erg cm}^{-2}$ ($E_{\gamma} \sim 2 \times 10^{46} \text{erg}$ at the distance of SN 2016coi).

6.1. Comparison to Breakout Models

Following Katz et al. (2012) (and references therein), the expected shock breakout energy is $E_{BO} = 8\pi R_*^2 v_0 c \kappa^{-1}$ (their Eq. 40), where R_* is the stellar radius, κ is the opacity and v_0 is the shock velocity at breakout. For SN 2016coi we assume $\kappa \sim 0.4 \text{cm}^2 \text{g}^{-1}$ and adopt $v_0 \approx 0.3c$ (i.e., a shock velocity at breakout similar to the maximum ejecta velocity as inferred from the X-ray observations, see Katz et al. 2012, their Eq. 25). For compact progenitors like WR stars with $R_* = 10^{11} \text{cm}$ we find $E_{BO} \approx 10^{44} \text{erg}$, significantly below the IPN sensitivity. *Fermi*-GBM and *Swift*-BAT are more sensitive and reach fluence limits of $\sim 4 \times 10^{-8} \text{erg cm}^{-2}$ and $\sim 6 \times 10^{-9} \text{erg cm}^{-2}$, respectively, corresponding to $E_{\gamma} \sim 2 \times 10^{45} \text{erg}$ and $E_{\gamma} \sim 2 \times 10^{44} \text{erg}$. The *Swift*-BAT threshold for detection is comparable to the expected E_{BO} . *Swift*-BAT observes $\sim 1/6$ of the sky with $\sim 90\%$ temporal duty cycle. It is thus possible that *Swift*-BAT missed the breakout pulse, or that the breakout pulse lies just below the *Swift*-BAT threshold of detection. For comparison the breakout pulse in SN 2008D showed $L_x \sim 10^{44} \text{erg s}^{-1}$ (0.3-10 keV) at peak with a duration of ~ 5 minutes.

More extended progenitors with radii $R_* = 10^{13}$ cm would lead to inferred $E_{BO} \approx 10^{48}$ erg. In this case however the spectrum of breakout pulse is expected to peak at lower frequencies < 1 keV which are not probed by the hard X-ray/ γ -ray observations presented here. A similar reasoning and conclusion apply if the radiation breakout occurred in a thick medium outside the star.

7. DISCUSSION

Our data analysis and modeling characterize SN 2016coi as an energetic H-stripped SN with (i) He in the ejecta, (ii) a broad bolometric light-curve, and (iii) luminous X-ray and radio emission. These three observables distinguish SN 2016coi from the rest of the population of known H-stripped SNe and directly map into properties of its progenitor star: a massive, well-mixed star that experienced substantial mass loss in the years preceding core-collapse. We discuss below the implications of these findings in the broader context of stellar progenitors of H-stripped SNe.

7.1. Broad Bolometric Light-Curve and Nebular Spectroscopy Indicate a Massive Progenitor

Among H-stripped SNe, SN 2016coi shows one of the broadest bolometric light-curves (Fig. 3), from which we infer $M_{ej} \sim 5 - 7 M_\odot$ (§2.2; Kumar et al. 2018; Prentice et al. 2018). This value is larger than the typical ejecta mass $M_{ej} \sim 2 - 3 M_\odot$ inferred for H-stripped SNe (e.g., Drouot et al. 2011; Bianco et al. 2014; Lyman et al. 2016; Taddia et al. 2018).

Other type Ic SNe with broad light-curves are SNe 2004aw (Taubenberger et al. 2006) and 2011bm (the broadest light curve in Fig. 3; Valenti et al. 2012), for which the inferred ejecta mass is 3.5–8.0 and 7–17 M_\odot , respectively. Additionally, SN 2004aw also displayed relatively high ejecta velocities ($v \sim 12000$ km/s⁻¹) around maximum light, similar to SN 2016coi. Interestingly, a tentative identification of He in the ejecta of SN 2004aw has also been reported based on NIR spectroscopy (Taubenberger et al. 2006).

Nebular spectroscopy of SN 2016coi provides additional constraints on the mass of its stellar progenitor. The relative abundances of different elements in a stellar envelope depend on the core mass. In particular, in the models by Fransson & Chevalier (1989) the ratio of the integrated fluxes of the [Ca II] $\lambda\lambda 7291, 7324$ doublet and the [O I] $\lambda\lambda 6300, 6364$ doublet can be used as an indicator of the progenitor core mass, with lower values signifying of more massive cores. This fact mainly results from two factors: first, in the models by Fransson & Chevalier (1989) the relative abundance Ca/O is lower for progenitors with a more massive core, producing a lower [Ca II]/[O I] flux ratio; second, in stars with a smaller core mass and with a stratified envelope like the ones in Fransson & Chevalier (1989) models, the Ca is more mixed within

the oxygen layers. Since Ca is a significantly more efficient coolant, this translates into more prominent [Ca II]/[O I] ratio. However, several other factors can play a role in determining the observed [Ca II]/[O I] flux ratio. Fransson & Chevalier (1989), for example, showed that higher densities of the ejecta (i.e., lower kinetic energies) would also lead to lower [Ca II]/[O I] flux ratios. Additionally, a high degree of mixing of the entire stellar envelope, where oxygen is more centrally located, also leads to a lower [Ca II]/[O I] flux ratio (as in this case cooling through oxygen would act as a competitor to calcium in the inner envelope). These factors make the observed [Ca II]/[O I] flux ratio a non-monotonic tracer of the stellar core-mass.

With these caveats in mind, the [Ca II]/[O I] flux ratio has been used in the past as a diagnostic for the progenitor star M_{ZAMS} in core-collapse SNe (e.g., Fransson & Chevalier 1987, 1989; Elmhamdi 2011; Kuncarayakti et al. 2015). We therefore compute this ratio as a function of time in SN 2016coi and show the results in Fig. 11. To build a homogeneous comparison sample, we retrieved late-time spectra of stripped-envelope SNe available from the literature⁸. We select all the SNe with observations at $t > 100$ days after explosion, and with at least one spectrum covering both the [O I] and the [Ca II] region. We focus on those SNe with a [Ca II]/[O I] ratio below 1.3. Our sample comprises 83 spectra from 29 different SNe. We then fit the line doublets with two Gaussian profiles (see Fig. 5). The position of the first centroid is kept as a free parameter, but the separation between the two lines of each doublet is kept fixed at the expected value.

From Fig. 11 it is clear that at very late phases SN 2016coi occupies the lower part of the plot, and at $t > 400$ d has the lowest [Ca II]/[O I] ratio, close to ~ 0.2 . For reference, Fransson & Chevalier (1989) found ratios of ~ 0.6 and ~ 5.6 for their 8 M_\odot and 4 M_\odot He-core progenitor models, respectively. This analysis independently supports the idea that SN 2016coi originated from a stellar progenitor with larger mass than the average progenitor of H-stripped core-collapse SNe. However, as described above, other factors can contribute to the observed [Ca II]/[O I] ratio, like mixing and ejecta densities. Indeed, the values measured by Fransson & Chevalier (1989) would become ~ 0.3 and ~ 1.6 for the same progenitor models as above, with lower explosion kinetic energies (~ 8 times higher densities).

Other SNe with low flux ratios (< 0.3) are the type Ib SN 1985F (Schlegel & Kirshner 1989; Elmhamdi et al. 2004), and the two type Ic SNe 1997B (spectra retrieved from the Asiago Supernova Archive) and 2004aw (Taubenberger et al.

⁸ The spectra were retrieved from WISeREP (<https://wiserep.weizmann.ac.il> Yaron & Gal-Yam 2012) and the OSC (<https://sne.space>; Guillochon et al. 2017).

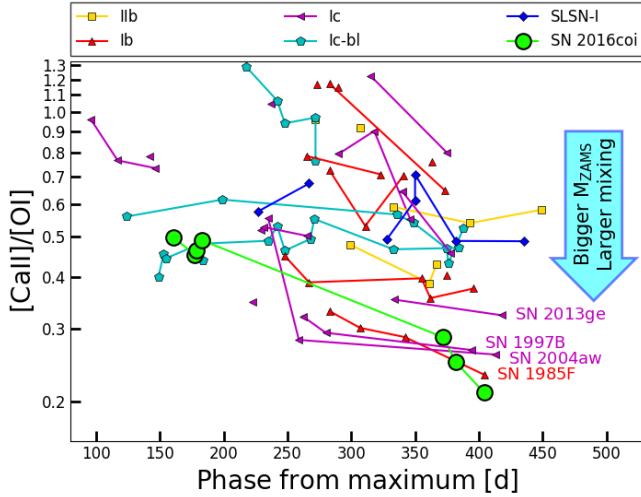


Figure 11. Comparison between the evolution of the $[\text{Ca II}]/[\text{O I}]$ $\lambda\lambda 7291,7324$ to $[\text{O I}] \lambda\lambda 6300,6364$ ratio for SN 2016coi and other type Ic and BL-Ic SNe. SN 2016coi is characterised by low $[\text{Ca II}]/[\text{O I}]$ ratio, suggesting a high M_{ZAMS} progenitor, with a high level of mixing at the time of explosion. Other events with a low ratio are SNe 1985F, 1997B and 2004aw. Measurements were performed depending on availability of late-time spectra retrievable from the literature (Gaskell et al. 1986; Filippenko & Sargent 1986; Filippenko et al. 1995; Barbon et al. 1999; Patat et al. 2001; Foley et al. 2003; Elmhamdi et al. 2004; Taubenberger et al. 2006; Tanaka et al. 2009; Taubenberger et al. 2009; Milisavljevic et al. 2010; Valenti et al. 2011; Silverman et al. 2012; Valenti et al. 2012; Benetti et al. 2011; Ben-Ami et al. 2014; Modjaz et al. 2014; Ergon et al. 2015; Kuncarayakti et al. 2015; Milisavljevic et al. 2015a,b; Smartt et al. 2015; Drout et al. 2016; Nicholl et al. 2016; Kangas et al. 2017; Taddia et al. 2019).

2006). Interestingly, at least two of these SNe also have broad light curves. The bolometric light-curve of SN 2004aw is very similar to SN 2016coi (Fig. 3), while SN 1985F has an even broader light curve, with a Δ_{15} in B -band of 0.52 mag (Tsvetkov 1986) ($\Delta_{15}=1.01$ mag for SN 2016coi Kumar et al. 2018). Unfortunately, SN 1997B was discovered after peak. Consistent with the caveats above, some SNe with broad light curve have large $[\text{Ca II}]/[\text{O I}]$ ratio (e.g., SN 2011bm, Lyman et al. 2016).

Based on the estimated $M_{ej} \sim 4-7 M_{\odot}$ (§2.2), and assuming a fiducial mass for the remnant compact object between $1.5 M_{\odot}$ (for a neutron star) and $3 M_{\odot}$ (for a black hole), we estimate a mass of the C+O stellar progenitor of SN 2016coi at the time of collapse of $\sim 6-10 M_{\odot}$. Similar values have been inferred for the progenitor of SN 2004aw, for which Mazzali et al. (2017) estimated a ZAMS mass of $\sim 23-30 M_{\odot}$.⁹ The actual value of the inferred ZAMS mass

⁹ The field of SN 2016coi was not serendipitously observed by HST before explosion, which prevents a constraining search for a progenitor star in pre-explosion images. The $\text{H}\alpha$ Galaxy Survey (James et al. 2004) observed

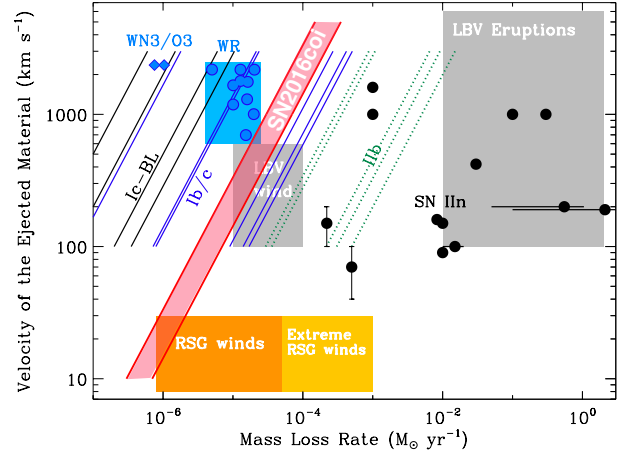


Figure 12. Constraints on the recent mass-loss history of SN 2016coi (red shaded area) in the context of observed mass-loss rates and wind velocities in massive stars. Here we conservatively plot the equipartition \dot{M} . The true SN 2016coi \dot{M} is ~ 10 times larger if $\epsilon_B = 0.01$. Galactic WR stars from Crowther 2007, WN3/O3 stars from Massey et al. 2015, red supergiants (RSGs) winds from de Jager et al. 1988; Marshall et al. 2004; van Loon et al. 2005. Typical locations of Luminous Blue Variable (LBV) winds and eruptions are from Smith 2014 and Smith & Owocki 2006. Black, blue and dotted green lines mark the sample of type Ic-BL, Ibc and IIB SNe from Drout et al. (2016). Inferred mass-loss rates for type-IIIn SNe are from Kiewe et al. (2012).

strongly depends on the adopted mass loss prescriptions (e.g., Smith 2014).

7.2. Luminous Radio and X-ray Emission from Large Progenitor Mass-loss before Explosion

The recent mass-loss history of the progenitor star in the centuries leading up to the explosion can be constrained with radio and X-ray observations, which sample the emission originating from the interaction between the fastest SN ejecta and the CSM. The resulting luminosity mainly depends on the shock velocity and on the environment density, with faster shocks and denser environments powering the most luminous radio and X-ray displays.

We compare the properties of SN 2016coi that we inferred in §4.2 and 5.2 to a sample of H-stripped SNe in Fig. 10. SNe with fast ejecta velocities like Ic-BL SNe (orange squares and triangles in Fig. 10) tend to be associated with low-density environments, while type IIB SNe are located within the densest circumstellar media. From the radio we inferred a shock velocity of $v_{sh} \sim 0.15c$ for SN 2016coi. This sub-

the field of SN 2016coi on June 6th, 2000. A compact source of $\text{H}\alpha$ emission is clearly detected $\sim 4.9''$ from the SN location, (yellow mark in Fig. 1). At the distance of SN 2016coi, this angular separation corresponds to a projected distance of 0.43 kpc. Prentice et al. (2018) estimated 0.375 kpc, using however a shorter distance to the host galaxy (see Table 1).

relativistic shock can be caused either by a lower shock velocity at breakout, or by a denser-than-average environment surrounding the progenitor. In the latter case, the CSM was sculpted by a prolonged enhanced mass-loss phase of the stellar progenitor in the years before stellar death. The environment of SN 2016coi is among the densest in the sample of type Ibc SNe. Assuming equipartition of energy, from the radio data we obtained a lower limit for the mass-loss of SN 2016coi of $\dot{M} \sim 3-4 \times 10^{-5} M_{\odot} \text{yr}^{-1}$ (for $v_w = 1000 \text{ km s}^{-1}$). X-ray analysis pushed this value even higher, with $\dot{M} \sim 1-2 \times 10^{-4} M_{\odot} \text{yr}^{-1}$. Such a large mass-loss rate is consistent with those associated with extreme line-driven winds in WR stars (Crowther 2007), as we show in Fig. 10-12. This result is also supported by the radio modelling, which showed that the post-explosion density profile of the outer ejecta is consistent with having originated from a compact object like a WR star. The inferred \dot{M} , if sustained for the entire $\sim 10^5 \text{ yr}$ duration of the WR phase, implies a total mass-loss of several M_{\odot} possibly sufficient to strip the progenitor star of a large fraction of its helium envelope even in the absence of interactions with a binary companion¹⁰. This scenario is consistent with the indication of a massive stellar progenitor of §7.1.

7.3. He Spectral Features as a Signature of Asymmetries?

The presence of He in SN 2016coi is supported by the comparison with the velocity profile of Si II $\lambda 6355$ (§3.2), and by the detailed spectral modeling of Prentice et al. (2018). He I lines are formed through non-thermal excitation and ionization (Lucy 1991), for example by γ -rays produced by the radioactive decay of ^{56}Ni and ^{56}Co . For this excitation channel to be effective, plumes of ^{56}Ni -rich material must have been able to reach the outer He-rich layers of the progenitor star of SN 2016coi, consistent with the results from our two-zone modeling of the bolometric emission from SN 2016coi in §2.2, and consistent with the results from recent 3D simulations of stellar explosions (e.g., Wongwathanarat et al. 2015) and studies of SN remnants (Milisavljevic & Fesen 2015). Indeed, models of Dessart et al. (2012) showed that a single plume of ^{56}Ni -rich material injected into the outer layers (e.g., in the form of a jet) is capable of producing weak He features. Alternatively, 3D simulations of neutrino-driven explosions have shown mixing instabilities that are capable of injecting ^{56}Ni - and Si-rich plumes to the higher velocities layers of the ejecta (e.g., Hammer et al. 2010). Indeed, we observed a very similar velocity evolution for Si II and He I, supporting this scenario. In their spectral modelling, Prentice et al. (2018) also showed that at early phases heavy ions were travelling at a very high speed; Fe II was the fastest species at

¹⁰ The measured mass-loss refers to the WR-phase of the progenitor, therefore little could be said about the process responsible for the stripping of its hydrogen envelope.

$26\,000 \text{ km s}^{-1}$. Also the Ca II showed similar high velocities, possibly hinting to some high velocity material coming from the progenitor core, as seen in GRB-SNe (e.g. Bufano et al. 2012; Toy et al. 2016; Ashall et al. 2019).

Among type Ic SNe with broad lines, SNe 2009bb and 2012ap have been reported to have signatures of He in their spectra¹¹ (Pignata et al. 2011; Milisavljevic et al. 2015b). Interestingly, SNe 2009bb and 2012ap are currently the only two cases of SNe with mildly relativistic ejecta not associated with a GRB (Soderberg et al. 2010b; Margutti et al. 2014; Chakraborti et al. 2015). This phenomenology has been suggested to be the result of a jet-driven stellar explosion where the jet fails to break through the stellar envelope (Morsony et al. 2007; Lazzati et al. 2012; Margutti et al. 2014). In this picture, relativistic SNe and GRBs are intrinsically different types of explosions, as opposed to similar explosions viewed from different perspectives. In relativistic SNe the jet is possibly choked by the more extended stellar envelope, but manages to “transport” some ^{56}Ni -rich material outwards and then excites some residual He that the stellar progenitor failed to shed before stellar death (Maeda et al. 2002; Suzuki & Maeda 2018; Izzo et al. 2019).

We speculate that a similar scenario applies to SN 2016coi, for which the lack of evidence for mildly relativistic ejecta can be explained as the result of a jet that died deep inside the star, leaving no imprint on the dynamics of the fastest ejected material, yet accelerating the inner layers to velocities larger than in normal type Ic SNe (Fig. 6), and at the same time injecting metal-rich material into the outer layer of the ejecta. In this context, the difference between normal type Ibc SNe and those with large ejecta velocities (including type Ic-BL and SN 2016coi) would be ascribed to the absence/presence of a jet at the time of core-collapse (Khokhlov et al. 1999; Granot & Ramirez-Ruiz 2004; Wheeler & Akiyama 2010; Lazzati et al. 2012; Nagakura et al. 2012; Margutti et al. 2014; Soker 2016).

8. SUMMARY AND CONCLUSIONS

We present the results of a multi-wavelength, γ -rays to radio campaign on the peculiar SN 2016coi (Yamanaka et al. 2017; Kumar et al. 2018; Prentice et al. 2018) during its first 420 days of evolution. Our findings can be summarized as follows:

- From extensive UV/optical/NIR photometry we derive a broad bolometric light-curve (Fig. 3), which is suggestive of a larger-than-average explosion ejecta mass. From our two-zone modeling we infer $M_{e,j,tot} \sim 4-7 M_{\odot}$ (consistent with previous findings by Kumar

¹¹ There is also a disputed claim of He in SN 1998bw (Patat et al. 2001), and in the more recent SN 2017iuk (Izzo et al. 2019).

et al. 2018), with a larger fraction of ^{56}Ni per unit mass in the outer part of the ejecta. We also constrain a total kinetic energy of $E_k \sim (7-8) \times 10^{51}$ erg.

- Our spectroscopic analysis supports the presence of He in the SN ejecta, confirming the previous findings by Yamanaka et al. (2017), Kumar et al. (2018) and Prentice et al. (2018). We furthermore find a low $[\text{Ca II}]_{\lambda\lambda 7291,7324}$ to $[\text{O I}]_{\lambda\lambda 6300,6364}$ ratio, suggestive of a large progenitor core mass at the time of collapse.
- SN 2016coi is a luminous source of radio and X-rays, which result from the propagation of a sub-relativistic blast wave with $v \sim 0.15c$ into a dense environment sculpted by sustained mass-loss from the progenitor star before core-collapse. We infer a lower limit on the mass-loss rate of $\dot{M} \sim (3-4) \times 10^{-5} M_{\odot} \text{yr}^{-1}$ (for wind velocity $v_w = 1000 \text{km s}^{-1}$ and assuming energy equipartition), significantly larger than in type Ic-BL SNe.
- Radio modelling also revealed a phase of higher mass-loss rate lasting until ~ 30 years before explosion. Additionally, we inferred a post-explosion density profile of the outer ejecta compatible with the explosion of a compact star (e.g., a WR, as opposed to extended progenitors like red and yellow supergiant stars).
- We investigated the presence of a high-energy prompt pulse of emission in the γ -rays. From our analysis we can rule out a SN-associated shock breakout pulse with energy $E_{\gamma} > 2 \times 10^{46}$ erg, consistent with the theoretical expectations of shock break out from WR stars or from extended winds.

The emerging picture is that of a massive compact progenitor star that was able to retain some He until collapse, despite the heavy mass loss experienced in the years leading up to stellar demise. The combination of (i) large ejecta mass and (ii) large mass-loss in a H-stripped core-collapse SN with (iii) weak He features in the spectra, set SN 2016coi apart from all SNe with similar data coverage and quality in the literature. We speculate that the energetic SN 2016coi might be the result of a failed jet that was choked by the extended envelope mass of its progenitor star, in analogy with the relativistic type Ic-BL SNe 2009bb and 2012ap for which He has been identified in the ejecta. It is possible that this picture of a jet-driven explosion where the jet has been choked while trying to pierce through the He-rich stellar envelope extends to the entire class of type Ic-BL SNe that are not associated with GRBs. Future observing campaigns of type Ic-BL SNe with coordinated optical and NIR spectroscopy will reveal if traces of He in type Ic-BL SNe are more common than currently thought.

ACKNOWLEDGMENTS

We thank N. Morrell for observing at du Pont telescope, and E. Falco for observing at FLWO.

ASAS-SN is supported by the Gordon and Betty Moore Foundation through grant GBMF5490 to the Ohio State University and NSF grant AST-1515927. Development of ASAS-SN has been supported by NSF grant AST-0908816, the Mt. Cuba Astronomical Foundation, the Center for Cosmology and AstroParticle Physics at the Ohio State University, the Chinese Academy of Sciences South America Center for Astronomy (CASSACA), the Villum Foundation, and George Skestos. We thank the Las Cumbres Observatory (LCOGT) and its staff for its continuing support of the ASAS-SN project. The Liverpool Telescope is operated on the island of La Palma by Liverpool John Moores University in the Spanish Observatorio del Roque de los Muchachos of the Instituto de Astrofísica de Canarias with financial support from the UK Science and Technology Facilities Council. Based on observations made with the Nordic Optical Telescope Scientific Association at the Observatorio Roque de los Muchachos, La Palma, Spain, of the Instituto de Astrofísica de Canarias. Partially based on observations obtained with Copernico 1.82m Telescope (Asiago) operated by INAF Osservatorio Astronomico di Padova. This work makes use of data gathered with the 6.5-m Magellan Telescopes, at Las Campanas Observatory in Chile. Based on observations obtained with XMM-Newton, an ESA science mission with instruments and contributions directly funded by ESA Member States and NASA. We acknowledge the use of public data from the Swift data archive. This work made use of the data products generated by the NYU SN group, and released under DOI:10.5281/zenodo.58766, available at <https://github.com/nyusngroup/SESNTemple/>. This work has made use of the Weizmann Interactive Supernova Data Repository (<https://wiserep.weizmann.ac.il>). This work has made use of the Berkeley Supernova Database (<http://heracles.astro.berkeley.edu/sndb/>). This research has made use of the NASA/IPAC Extragalactic Database (NED), which is operated by the Jet Propulsion Laboratory, California Institute of Technology, under contract with NASA. The National Radio Astronomy Observatory is a facility of the National Science Foundation operated under cooperative agreement by Associated Universities, Inc. The RM group at Northwestern is partially supported by the National Aeronautics and Space Administration through Chandra Award Number GO6-17053A issued by the Chandra X-ray Center, which is operated by the Smithsonian Astrophysical Observatory for and on behalf of the National Aeronautics Space Administration under contract NAS8-03060, the Swift Guest Investigator program, NASA Grants NNX17AD82G and 80NSSC18K0575 and the XMM Guest Investigator pro-

gram, NASA Grant NNX16AT58G. SD and PC acknowledge Project 11573003 supported by NSFC. This research uses data obtained through the Telescope Access Program (TAP), which has been funded by the National Astronomical Observatories of China, the Chinese Academy of Sciences, and the Special Fund for Astronomy from the Ministry of Finance. KH is grateful for support under the Fermi Guest Investigator program, NASA Grant NNX15AU74G. Support for JLP is provided in part by FONDECYT through the grant 1191038 and by the Ministry of Economy, Development, and Tourism's Millennium Science Initiative through grant IC120009, awarded to The Millennium Institute of Astrophysics, MAS. LT and SB are partially supported by PRIN INAF 2017 "Towards the SKA and CTA era: discovery, localisation and physics of transient sources (PI M. Giroletti)." MS is supported by a generous grant (13261) from VILLUM

FONDEN and a project grant (8021-00170B) from the Independent Research Fund Denmark. NER acknowledges support from the Spanish MICINN grant ESP2017-82674-R and FEDER funds. CG is supported by a VILLUM FONDEN Investigator grant (project number 16599). JH acknowledges financial support from the Finnish Cultural Foundation.

Facility: ASAS-SN, Liverpool Telescope, Neil Gehrels *Swift* Observatory, XMM-Newton, Nordic Optical Telescope, Multiple Mirror Telescope, Rapid Eye Mount, 1.82m Copernico, 1.22m Galileo, du Pont Telescope, Large Binocular Telescope, Magellan, Telescopio Nazionale Galileo, Tillinghast 1.5m, Las Cumbres Observatory, DEMONEXT, WHO 1m (Weihai Observatory), T50 (OAUV), Gem (University of Iowa).

REFERENCES

- Arnett, W. D. 1982, *ApJ*, 253, 785
- Ashall, C., et al. 2019, *MNRAS*, 1522
- Barbon, R., Buondi, V., Cappellaro, E., & Turatto, M. 1999, *A&AS*, 139, 531
- Begelman, M. C., & Sarazin, C. L. 1986, *ApJL*, 302, L59
- Ben-Ami, S., et al. 2012, *ApJL*, 760, L33
- Ben-Ami, S., et al. 2014, *ApJ*, 785, 37
- Benetti, S., et al. 2011, *MNRAS*, 411, 2726
- Berger, E., Kulkarni, S. R., & Chevalier, R. A. 2002, *ApJL*, 577, L5
- Bersten, M. C., et al. 2014a, *AJ*, 148, 68
- Bersten, M. C., et al. 2014b, *AJ*, 148, 68
- Bianco, F. B., et al. 2014, *ApJS*, 213, 19
- Björnsson, C.-I., & Fransson, C. 2004, *ApJ*, 605, 823
- Brown, P. J., Breeveld, A. A., Holland, S., Kuin, P., & Pritchard, T. 2014, *Ap&SS*, 354, 89
- Brown, P. J., et al. 2009, *AJ*, 137, 4517
- Bufano, F., et al. 2012, *ApJ*, 753, 67
- Burrows, D. N., et al. 2005, *SSRv*, 120, 165
- Cao, Y., et al. 2013, *ApJL*, 775, L7
- Caprioli, D. 2012, *JCAP*, 7, 038
- Chakraborti, S., Ray, A., Soderberg, A. M., Loeb, A., & Chandra, P. 2011, *Nature Communications*, 2
- Chakraborti, S., et al. 2015, *ApJ*, 805, 187
- Chakraborti, S., et al. 2014, *ArXiv e-prints*
- Chandra, P., & Frail, D. A. 2012, *ApJ*, 746, 156
- Chevalier, R. A. 1982, *ApJ*, 258, 790
- Chevalier, R. A. 1998, *ApJ*, 499, 810
- Chevalier, R. A., & Fransson, C. 2006, *ApJ*, 651, 381
- Chevalier, R. A., & Li, Z.-Y. 2000, *ApJ*, 536, 195
- Chonis, T. S., & Gaskell, C. M. 2008, *AJ*, 135, 264
- Clocchiatti, A., Wheeler, J. C., Benetti, S., & Frueh, M. 1996, *ApJ*, 459, 547
- Corsi, A., et al. 2014, *ApJ*, 782, 42
- Crowther, P. A. 2007, *ARA&A*, 45, 177
- Crumley, P., Caprioli, D., Markoff, S., & Spitkovsky, A. 2019, *MNRAS*, 485, 5105
- de Jager, C., Nieuwenhuijzen, H., & van der Hucht, K. A. 1988, *A&AS*, 72, 259
- Dessart, L., Hillier, D. J., Li, C., & Woosley, S. 2012, *MNRAS*, 424, 2139
- Dessart, L., Hillier, D. J., Livne, E., Yoon, S.-C., Woosley, S., Waldman, R., & Langer, N. 2011, *MNRAS*, 414, 2985
- Dessart, L., Hillier, D. J., Woosley, S., Livne, E., Waldman, R., Yoon, S.-C., & Langer, N. 2015, *MNRAS*, 453, 2189
- Drout, M. R., et al. 2016, *ApJ*, 821, 57
- Drout, M. R., et al. 2011, *ApJ*, 741, 97
- Eldridge, J. J., Fraser, M., Maund, J. R., & Smartt, S. J. 2015, *MNRAS*, 446, 2689
- Eldridge, J. J., Fraser, M., Smartt, S. J., Maund, J. R., & Crockett, R. M. 2013, *MNRAS*, 436, 774
- Elias-Rosa, N., et al. 2016, *The Astronomer's Telegram*, 9090
- Elias-Rosa, N., et al. 2013, *MNRAS*, 436, L109
- Elmhamdi, A. 2011, *AcA*, 61, 179
- Elmhamdi, A., Danziger, I. J., Cappellaro, E., Della Valle, M., Gouiffes, C., Phillips, M. M., & Turatto, M. 2004, *A&A*, 426, 963
- Elmhamdi, A., et al. 2003, *MNRAS*, 338, 939
- Ensmann, L. M., & Woosley, S. E. 1988, *ApJ*, 333, 754
- Ergon, M., et al. 2015, *A&A*, 580, A142
- Filippenko, A. V. 1997, *ARA&A*, 35, 309
- Filippenko, A. V., et al. 1995, *ApJL*, 450, L11
- Filippenko, A. V., & Sargent, W. L. W. 1986, *AJ*, 91, 691
- Foley, R. J., et al. 2003, *PASP*, 115, 1220
- Fransson, C., & Björnsson, C.-I. 1998, *ApJ*, 509, 861

- Fransson, C., & Chevalier, R. A. 1987, *ApJL*, 322, L15
- Fransson, C., & Chevalier, R. A. 1989, *ApJ*, 343, 323
- Fransson, C., Lundqvist, P., & Chevalier, R. A. 1996, *ApJ*, 461, 993
- Gal-Yam, A. 2017, *Observational and Physical Classification of Supernovae*, ed. A. W. Alsabti & P. Murdin 195
- Gal-Yam, A., et al. 2005, *ApJL*, 630, L29
- Gaskell, C. M., Cappellaro, E., Dinerstein, H. L., Garnett, D. R., Harkness, R. P., & Wheeler, J. C. 1986, *ApJL*, 306, L77
- Gehrels, N., et al. 2004, *ApJ*, 611, 1005
- Georgy, C., Meynet, G., Walder, R., Folini, D., & Maeder, A. 2009, *A&A*, 502, 611
- Granot, J., & Ramirez-Ruiz, E. 2004, *ApJL*, 609, L9
- Groh, J. H., Georgy, C., & Ekström, S. 2013, *A&A*, 558, L1
- Guillochon, J., Parrent, J., Kelley, L. Z., & Margutti, R. 2017, *ApJ*, 835, 64
- Hamann, W.-R., Gräfener, G., & Liermann, A. 2006, *A&A*, 457, 1015
- Hammer, N. J., Janka, H.-T., & Müller, E. 2010, *ApJ*, 714, 1371
- Holoien, T. W.-S., et al. 2016, *The Astronomer's Telegram*, 9086
- Horesh, A., et al. 2013, *MNRAS*, 436, 1258
- Hu, Y., Deng, L., de Grijs, R., & Liu, Q. 2011, *PASP*, 123, 107
- Immler, S., Wilson, A. S., & Terashima, Y. 2002, *ApJL*, 573, L27
- Izzo, L., et al. 2019, *arXiv e-prints*
- James, P. A., et al. 2004, *A&A*, 414, 23
- Kalberla, P. M. W., Burton, W. B., Hartmann, D., Arnal, E. M., Bajaja, E., Morras, R., & Pöppel, W. G. L. 2005, *A&A*, 440, 775
- Kamble, A., et al. 2016, *ApJ*, 818, 111
- Kamble, A., et al. 2014, *ApJ*, 797, 2
- Kangas, T., et al. 2017, *MNRAS*, 469, 1246
- Katz, B., Sapir, N., & Waxman, E. 2012, *ApJ*, 747, 147
- Khokhlov, A. M., Höflich, P. A., Oran, E. S., Wheeler, J. C., Wang, L., & Chtchelkanova, A. Y. 1999, *ApJL*, 524, L107
- Kiewe, M., et al. 2012, *ApJ*, 744, 10
- Kilpatrick, C. D., et al. 2018, *MNRAS*, 480, 2072
- Krauss, M. I., et al. 2012, *ApJL*, 750, L40
- Kumar, B., Singh, A., Srivastav, S., Sahu, D. K., & Anupama, G. C. 2018, *MNRAS*, 473, 3776
- Kuncarayakti, H., et al. 2015, *A&A*, 579, A95
- Lazzati, D., Morsony, B. J., Blackwell, C. H., & Begelman, M. C. 2012, *ApJ*, 750, 68
- Lucy, L. B. 1991, *ApJ*, 383, 308
- Lyman, J. D., Bersier, D., James, P. A., Mazzali, P. A., Eldridge, J. J., Fraser, M., & Pian, E. 2016, *MNRAS*, 457, 328
- Maeda, K., et al. 2008, *Science*, 319, 1220
- Maeda, K., Mazzali, P. A., Deng, J., Nomoto, K., Yoshii, Y., Tomita, H., & Kobayashi, Y. 2003, *ApJ*, 593, 931
- Maeda, K., Nakamura, T., Nomoto, K., Mazzali, P. A., Patat, F., & Hachisu, I. 2002, *ApJ*, 565, 405
- Maeda, K., Nomoto, K., Mazzali, P. A., & Deng, J. 2006, *ApJ*, 640, 854
- Maeder, A. 1981, *A&A*, 99, 97
- Margutti, R., et al. 2017, *ApJ*, 835, 140
- Margutti, R., et al. 2014, *ApJ*, 797, 107
- Margutti, R., et al. 2012, *ApJ*, 751, 134
- Margutti, R., et al. 2013, *MNRAS*, 428, 729
- Marshall, J. R., van Loon, J. T., Matsuura, M., Wood, P. R., Zijlstra, A. A., & Whitelock, P. A. 2004, *MNRAS*, 355, 1348
- Massey, P., Neugent, K. F., & Morrell, N. 2015, *ApJ*, 807, 81
- Mattila, S., et al. 2016, *The Astronomer's Telegram*, 8992
- Matzner, C. D., & McKee, C. F. 1999, *ApJ*, 510, 379
- Maund, J. R., Smartt, S. J., & Schweizer, F. 2005, *ApJL*, 630, L33
- Mazzali, P. A., Sauer, D. N., Pian, E., Deng, J., Prentice, S., Ben Ami, S., Taubenberger, S., & Nomoto, K. 2017, *MNRAS*, 469, 2498
- McMullin, J. P., Waters, B., Schiebel, D., Young, W., & Golap, K. 2007, in *Astronomical Society of the Pacific Conference Series*, Vol. 376, *Astronomical Data Analysis Software and Systems XVI*, ed. R. A. Shaw, F. Hill, & D. J. Bell, 127
- Milisavljevic, D., & Fesen, R. A. 2015, *Science*, 347, 526
- Milisavljevic, D., Fesen, R. A., Gerardy, C. L., Kirshner, R. P., & Challis, P. 2010, *ApJ*, 709, 1343
- Milisavljevic, D., et al. 2015a, *ApJ*, 815, 120
- Milisavljevic, D., et al. 2015b, *ApJ*, 799, 51
- Milisavljevic, D., et al. 2013, *ApJL*, 770, L38
- Modjaz, M., et al. 2014, *AJ*, 147, 99
- Modjaz, M., Kirshner, R. P., Blondin, S., Challis, P., & Matheson, T. 2008, *ApJL*, 687, L9
- Modjaz, M., Liu, Y. Q., Bianco, F. B., & Graur, O. 2016, *ApJ*, 832, 108
- Mohan, N., & Rafferty, D. 2015, *PyBDSF: Python Blob Detection and Source Finder*, *Astrophysics Source Code Library*
- Morsony, B. J., Lazzati, D., & Begelman, M. C. 2007, *ApJ*, 665, 569
- Mould, J. R., et al. 2000, *ApJ*, 529, 786
- Nagakura, H., Suwa, Y., & Ioka, K. 2012, *ApJ*, 754, 85
- Nicholl, M., et al. 2016, *ApJL*, 828, L18
- Park, J., Caprioli, D., & Spitkovsky, A. 2015, *Physical Review Letters*, 114, 085003
- Parrent, J. T., Milisavljevic, D., Soderberg, A. M., & Parthasarathy, M. 2016, *ApJ*, 820, 75
- Patat, F., et al. 2001, *ApJ*, 555, 900
- Perna, R., Soria, R., Pooley, D., & Stella, L. 2008, *MNRAS*, 384, 1638
- Phillips, M. M., et al. 2013, *ApJ*, 779, 38
- Pignata, G., et al. 2011, *ApJ*, 728, 14
- Piro, A. L., & Nakar, E. 2013, *ApJ*, 769, 67
- Podsiadlowski, P., Joss, P. C., & Hsu, J. J. L. 1992, *ApJ*, 391, 246
- Pooley, D., & Lewin, W. H. G. 2004, *IAUC*, 8323, 2
- Poznanski, D., Prochaska, J. X., & Bloom, J. S. 2012, *MNRAS*, 426, 1465

- Prentice, S. J., et al. 2018, MNRAS, 478, 4162
- Roming, P. W. A., et al. 2005, SSRv, 120, 95
- Roming, P. W. A., et al. 2009, ApJL, 704, L118
- Ryder, S. D., Sadler, E. M., Subrahmanyan, R., Weiler, K. W., Panagia, N., & Stockdale, C. 2004, MNRAS, 349, 1093
- Schlafly, E. F., & Finkbeiner, D. P. 2011, ApJ, 737, 103
- Schlegel, E. M., & Kirshner, R. P. 1989, AJ, 98, 577
- Shappee, B. J., et al. 2014, ApJ, 788, 48
- Silverman, J. M., et al. 2012, MNRAS, 425, 1789
- Sironi, L., & Spitkovsky, A. 2011, ApJ, 726, 75
- Skrutskie, M. F., et al. 2006, AJ, 131, 1163
- Smartt, S. J., et al. 2015, A&A, 579, A40
- Smith, N. 2014, ARA&A, 52, 487
- Smith, N., Li, W., Filippenko, A. V., & Chornock, R. 2011, MNRAS, 412, 1522
- Smith, N., & Owocki, S. P. 2006, ApJL, 645, L45
- Soderberg, A. M., et al. 2008, Nature, 453, 469
- Soderberg, A. M., Brunthaler, A., Nakar, E., Chevalier, R. A., & Bietenholz, M. F. 2010a, ApJ, 725, 922
- Soderberg, A. M., et al. 2010b, Nature, 463, 513
- Soderberg, A. M., Kulkarni, S. R., Berger, E., Chevalier, R. A., Frail, D. A., Fox, D. B., & Walker, R. C. 2005, ApJ, 621, 908
- Soderberg, A. M., et al. 2006a, Nature, 442, 1014
- Soderberg, A. M., Nakar, E., Berger, E., & Kulkarni, S. R. 2006b, ApJ, 638, 930
- Soker, N. 2016, NewAR, 75, 1
- Soria, R., Pian, E., & Mazzali, P. A. 2004, A&A, 413, 107
- Stetson, P. B. 1987, PASP, 99, 191
- Suzuki, A., & Maeda, K. 2018, MNRAS, 478, 110
- Taddia, F., Sollerman, J., Fremling, C., Karamahmetoglu, E., Barbarino, C., Lunnan, R., West, S., & Gal-Yam, A. 2019, A&A, 621, A64
- Taddia, F., et al. 2018, A&A, 609, A136
- Takaki, K., et al. 2013, ApJL, 772, L17
- Tanaka, M., et al. 2009, ApJ, 700, 1680
- Taubenberger, S., et al. 2006, MNRAS, 371, 1459
- Taubenberger, S., et al. 2009, MNRAS, 397, 677
- Thomas, R. C., Nugent, P. E., & Meza, J. C. 2011, PASP, 123, 237
- Toy, V. L., et al. 2016, ApJ, 818, 79
- Tsvetkov, D. Y. 1986, Soviet Astronomy Letters, 12, 328
- Turatto, M., Benetti, S., & Cappellaro, E. 2003, in From Twilight to Highlight: The Physics of Supernovae, ed. W. Hillebrandt & B. Leibundgut, 200
- Valenti, S., et al. 2008, MNRAS, 383, 1485
- Valenti, S., et al. 2011, MNRAS, 416, 3138
- Valenti, S., et al. 2012, ApJL, 749, L28
- van Dyk, S. D., Weiler, K. W., Sramek, R. A., Rupen, M. P., & Panagia, N. 1994, ApJL, 432, L115
- Van Dyk, S. D., et al. 2018, ApJ, 860, 90
- van Loon, J. T., Cioni, M.-R. L., Zijlstra, A. A., & Loup, C. 2005, A&A, 438, 273
- Villanueva, S., Jr., Gaudi, B. S., Pogge, R. W., Eastman, J. D., Stassun, K. G., Trueblood, M., & Trueblood, P. 2018, PASP, 130, 015001
- Weiler, K. W., Panagia, N., Montes, M. J., & Sramek, R. A. 2002, ARA&A, 40, 387
- Wheeler, J. C., & Akiyama, S. 2010, New Astronomy, 54, 183
- Wheeler, J. C., Johnson, V., & Clocchiatti, A. 2015, MNRAS, 450, 1295
- Wongwathanarat, A., Müller, E., & Janka, H.-T. 2015, A&A, 577, A48
- Woosley, S. E., Langer, N., & Weaver, T. A. 1995, ApJ, 448, 315
- Xiang, D., et al. 2019, ApJ, 871, 176
- Yamanaka, M., et al. 2016, The Astronomer's Telegram, 9124
- Yamanaka, M., et al. 2017, ApJ, 837, 1
- Yaron, O., & Gal-Yam, A. 2012, PASP, 124, 668
- Yoon, S.-C., Woosley, S. E., & Langer, N. 2010, ApJ, 725, 940
- York, D. G., et al. 2000, AJ, 120, 1579

APPENDIX

Table A1. Telescopes and instruments used for the photometric follow-up of SN 2016coi. The acronyms reported in the first column are those used in Tables A2–A5.

Code	Telescope	Instrument	Pixel size	FoV	Filters
ASA	14cm Brutus ^a	Fairchild CCD3041	7.8''	4.47° × 4.47°	V
RK	25cm Meade SCT ^b	Apogee AP-47	1.02''	17.4' × 17.4'	BVRI
JB	43cm PlaneWave CDK ^c	SBIG STL-6303	0.63''	34' × 22'	BVri
GS	43cm PlaneWave CDK ^d	SBIG STXL-11002	0.63''	42' × 28'	BV
T50	T50 ^e	ProLine PL16801	0.54''	36.9' × 36.9'	BVri
Gem	Gem ^f	SBIG 6303e	1.08''	27.6' × 18.4'	BVgri
DEM	51cm PlaneWave CDK ^g	Fairchild CCD3041	0.90''	30.7' × 30.7'	BVri
WHO	WHO 1m telescope ^h	Andor iKon-L DZ936-N	0.35''	12' × 12'	BVri
LCOGT	Las Cumbres Observatory (LCOGT)	Sinistro	0.40''	26' × 26'	BVgri
1.82	1.82m Copernico	AFOSC	0.52''	8.7' × 8.7'	UBVRIugriz
REM	Rapid Eye Mount (REM)	REM-IR	0.58''	9.1' × 9.1'	JHK
		ROSS2	1.22''	9.9' × 9.9'	griz
LT	Liverpool Telescope	IO:O	0.30''	10' × 10'	BVgriz
		IO:I	0.18''	6.3' × 6.3'	H
NOT	Nordic Optical Telescope (NOT)	NOTCam	0.24''	4' × 4'	JHK
		ALFOSC	0.19''	6.4' × 6.4'	UBVugriz
MMT	Multiple Mirror Telescope (MMT)	MMTCam	0.08''	2.7' × 2.7'	gri
UVOT	Ultraviolet Optical Telescope (UVOT) ⁱ	MIC ^j	0.50''	17' × 17'	UV-W1,M2,W2 UBV

^aOperated by the ASAS-SN team (Shappee et al. 2014).^bOperated by R. A. Koff at Antelope Hills Observatory, Bennett, CO, USA.^cOperated by Joseph Brimacombe at New Mexico Skies, New Mexico, USA.^dOperated by Geoffrey Stone at Sierra Remote Observatories, Auberry, CA, USA.^eOperated by the Astronomical Observatory of the University of Valencia (OAUV) at Aras de los Olmos, Valencia, Spain.^fOperated by the University of Iowa at Iowa Robotic Observatory.^gOperated by DEMONEXT (Villanueva et al. 2018).^hOperated by the Weihai Observatory of Shandong University, China.ⁱon board the Neil Gehrels *Swift* Observatory.^jMicrochannel plate intensified CCD.

Table A2. *ugriz* photometry.

MJD	<i>u</i> (mag)	<i>g</i> (mag)	<i>r</i> (mag)	<i>i</i> (mag)	<i>z</i> (mag)	Instrument
57536.14	–	–	15.20 (0.04)	15.46 (0.03)	–	NOT
57536.40	–	15.80 (0.05)	15.17 (0.05)	15.55 (0.10)	–	Gem
57537.15	–	–	14.84 (0.15)	15.09 (0.11)	–	NOT
57537.41	–	15.43 (0.04)	14.87 (0.05)	15.25 (0.10)	–	Gem
57538.39	–	15.17 (0.04)	14.63 (0.05)	15.03 (0.10)	–	Gem
57539.39	–	14.93 (0.04)	14.43 (0.05)	14.83 (0.10)	–	Gem
57539.76	–	–	–	14.69 (0.16)	–	WHO
57540.17	15.68 (0.03)	14.76 (0.03)	14.25 (0.03)	14.61 (0.02)	14.56 (0.03)	LT
57540.76	–	–	14.14 (0.05)	14.59 (0.04)	–	WHO
57541.40	–	14.59 (0.04)	14.14 (0.05)	14.54 (0.10)	–	Gem
57541.75	–	–	14.11 (0.06)	14.48 (0.06)	–	WHO
57542.21	15.61 (0.04)	14.47 (0.02)	14.04 (0.03)	14.39 (0.03)	14.24 (0.02)	LT
57542.38	–	–	13.99 (0.03)	14.39 (0.06)	–	DEM
57543.37	–	14.35 (0.05)	13.90 (0.06)	14.32 (0.10)	–	Gem
57543.41	–	–	13.89 (0.03)	14.30 (0.06)	–	DEM
57544.37	–	14.29 (0.04)	13.86 (0.05)	14.22 (0.10)	–	Gem
57544.44	–	–	13.80 (0.03)	14.23 (0.06)	–	DEM
57545.34	–	–	13.74 (0.03)	14.17 (0.06)	–	DEM
57545.39	–	14.21 (0.05)	13.77 (0.07)	14.15 (0.10)	–	Gem
57546.22	–	–	–	14.20 (0.10)	–	NOT
57546.29	–	14.22 (0.09)	13.70 (0.06)	14.13 (0.13)	–	REM
57546.39	–	14.19 (0.04)	13.72 (0.06)	14.09 (0.10)	–	Gem
57546.43	–	–	13.68 (0.06)	14.10 (0.06)	–	LCOGT
57546.44	–	–	13.68 (0.03)	14.10 (0.06)	–	DEM
57547.33	–	–	13.65 (0.03)	14.07 (0.06)	–	DEM
57547.37	–	–	13.65 (0.07)	14.06 (0.10)	–	REM
57547.37	–	14.16 (0.04)	13.71 (0.05)	14.08 (0.10)	–	Gem
57548.38	–	–	13.62 (0.08)	14.04 (0.11)	–	REM
57549.42	–	14.15 (0.06)	13.59 (0.06)	14.02 (0.11)	–	REM
57549.43	–	–	13.60 (0.03)	13.96 (0.05)	–	LCOGT
57550.41	–	–	13.62 (0.03)	13.97 (0.05)	–	LCOGT
57550.44	–	–	13.59 (0.06)	13.95 (0.12)	–	REM
57551.19	15.92 (0.06)	14.19 (0.02)	13.54 (0.04)	13.97 (0.04)	13.69 (0.03)	LT
57551.42	–	–	13.56 (0.04)	13.93 (0.06)	–	DEM
57552.06	15.96 (0.06)	14.19 (0.03)	13.58 (0.02)	13.95 (0.03)	13.64 (0.03)	LT
57552.35	–	14.22 (0.04)	13.62 (0.05)	13.95 (0.10)	–	Gem
57553.17	16.10 (0.06)	14.29 (0.05)	13.59 (0.06)	13.89 (0.06)	13.55 (0.04)	LT
57553.19	16.10 (0.08)	–	–	–	–	NOT
57553.35	–	14.26 (0.05)	13.62 (0.05)	13.95 (0.10)	–	Gem
57553.37	–	–	13.57 (0.03)	13.92 (0.06)	–	DEM
57554.12	16.23 (0.04)	14.32 (0.04)	13.64 (0.07)	13.95 (0.06)	13.55 (0.04)	LT
57554.42	–	–	13.57 (0.03)	–	–	DEM
57555.24	–	14.39 (0.25)	13.59 (0.10)	13.91 (0.11)	–	REM
57556.37	–	14.43 (0.04)	13.67 (0.05)	13.95 (0.10)	–	Gem
57557.03	16.39 (0.03)	14.44 (0.10)	13.70 (0.07)	– 13.54 (0.07)	1.82	
57557.13	16.59 (0.04)	14.45 (0.02)	13.58 (0.04)	13.91 (0.03)	13.59 (0.03)	LT
57557.22	–	–	13.62 (0.08)	13.91 (0.12)	–	REM
57557.43	–	–	13.64 (0.04)	13.90 (0.05)	–	LCOGT
57558.10	16.70 (0.04)	14.55 (0.02)	13.65 (0.03)	13.98 (0.03)	13.69 (0.04)	LT
57558.23	–	–	13.68 (0.06)	13.93 (0.15)	–	REM

Table A2. Continued: *ugriz* photometry.

MJD	<i>u</i> (mag)	<i>g</i> (mag)	<i>r</i> (mag)	<i>i</i> (mag)	<i>z</i> (mag)	Instrument
57558.40	–	–	13.68 (0.06)	13.94 (0.11)	–	LCOGT
57559.07	16.89 (0.05)	14.60 (0.03)	13.65 (0.03)	13.95 (0.03)	13.59 (0.03)	LT
57559.24	–	–	13.70 (0.08)	13.90 (0.13)	–	REM
57559.44	–	–	13.73 (0.03)	13.97 (0.05)	–	LCOGT
57560.30	–	14.76 (0.35)	13.74 (0.08)	13.94 (0.11)	–	REM
57560.40	–	–	–	14.00 (0.05)	–	LCOGT
57561.06	17.22 (0.06)	14.72 (0.03)	13.81 (0.06)	14.04 (0.06)	13.70 (0.03)	LT
57561.30	–	–	13.75 (0.08)	13.92 (0.14)	–	REM
57562.07	17.26 (0.07)	14.81 (0.10)	13.76 (0.10)	14.02 (0.09)	13.48 (0.08)	1.82
57562.11	17.27 (0.05)	14.90 (0.02)	13.72 (0.04)	14.05 (0.03)	13.61 (0.03)	LT
57562.40	–	–	13.81 (0.06)	14.00 (0.07)	–	LCOGT
57563.13	17.47 (0.05)	14.99 (0.03)	13.86 (0.05)	14.09 (0.04)	13.90 (0.07)	LT
57563.43	–	–	–	14.05 (0.05)	–	LCOGT
57566.32	–	–	14.00 (0.07)	14.12 (0.11)	–	REM
57566.41	–	–	14.01 (0.03)	14.18 (0.05)	–	LCOGT
57567.33	–	–	14.03 (0.06)	14.14 (0.13)	–	REM
57567.40	–	–	14.07 (0.03)	14.22 (0.05)	–	LCOGT
57568.15	17.93 (0.05)	15.34 (0.02)	14.04 (0.03)	14.19 (0.03)	13.84 (0.02)	LT
57568.35	–	–	14.08 (0.09)	14.16 (0.11)	–	REM
57568.40	–	–	14.12 (0.03)	14.24 (0.05)	–	LCOGT
57569.08	18.05 (0.08)	15.38 (0.01)	14.03 (0.03)	14.21 (0.03)	13.90 (0.03)	LT
57569.36	–	–	14.13 (0.07)	14.22 (0.12)	–	REM
57570.17	18.06 (0.05)	15.46 (0.03)	14.15 (0.04)	14.28 (0.03)	13.85 (0.03)	LT
57572.98	–	–	14.31 (0.04)	14.39 (0.06)	–	LCOGT
57573.02	18.14 (0.07)	15.67 (0.14)	14.33 (0.11)	14.37 (0.11)	–	NOT
57576.09	–	–	14.47 (0.04)	14.49 (0.06)	–	LCOGT
57577.10	18.46 (0.05)	15.71 (0.04)	14.54 (0.05)	14.51 (0.03)	14.05 (0.03)	LT
57577.13	–	–	14.51 (0.04)	14.53 (0.06)	–	LCOGT
57578.13	–	–	14.56 (0.04)	14.56 (0.06)	–	LCOGT
57579.11	18.44 (0.06)	15.79 (0.03)	14.52 (0.03)	14.63 (0.03)	14.14 (0.03)	LT
57580.06	–	–	14.64 (0.04)	14.61 (0.06)	–	LCOGT
57580.11	18.48 (0.05)	15.88 (0.03)	14.59 (0.04)	14.67 (0.03)	14.26 (0.04)	LT
57581.10	18.48 (0.04)	15.99 (0.03)	14.58 (0.04)	14.63 (0.05)	14.13 (0.03)	LT
57581.13	–	–	14.66 (0.04)	14.65 (0.06)	–	LCOGT
57582.13	–	–	14.73 (0.04)	14.70 (0.05)	–	LCOGT
57583.13	–	–	14.75 (0.04)	14.72 (0.06)	–	LCOGT
57584.11	–	15.98 (0.03)	14.79 (0.04)	14.75 (0.07)	–	LCOGT
57585.29	–	–	14.82 (0.04)	14.76 (0.06)	–	LCOGT
57586.13	–	–	14.85 (0.05)	14.77 (0.08)	–	LCOGT
57586.13	18.61 (0.04)	16.15 (0.04)	14.80 (0.05)	14.79 (0.03)	14.31 (0.02)	LT
57587.34	–	–	14.89 (0.04)	14.83 (0.07)	–	LCOGT
57588.13	18.66 (0.04)	16.01 (0.02)	14.93 (0.03)	14.87 (0.02)	14.36 (0.03)	LT
57590.10	18.93 (0.15)	16.14 (0.15)	14.95 (0.13)	14.84 (0.08)	–	NOT
57591.32	–	–	14.99 (0.06)	14.92 (0.08)	–	LCOGT
57593.07	–	–	15.01 (0.07)	14.97 (0.05)	–	T50
57593.11	18.78 (0.05)	16.16 (0.04)	14.97 (0.03)	14.98 (0.03)	14.42 (0.03)	LT
57594.05	–	–	15.11 (0.08)	15.04 (0.07)	–	T50
57594.70	–	–	15.11 (0.04)	15.00 (0.06)	–	LCOGT
57596.01	18.86 (0.06)	16.22 (0.05)	15.05 (0.05)	15.07 (0.03)	14.52 (0.08)	LT
57596.07	–	–	15.17 (0.06)	15.06 (0.04)	–	T50

Table A2. *Continued: ugriz photometry.*

MJD	<i>u</i> (mag)	<i>g</i> (mag)	<i>r</i> (mag)	<i>i</i> (mag)	<i>z</i> (mag)	Instrument
57597.07	–	–	15.16 (0.28)	–	–	T50
57597.73	–	–	15.18 (0.04)	15.07 (0.06)	–	LCOGT
57598.20	18.80 (0.04)	16.29 (0.03)	15.13 (0.04)	15.08 (0.04)	14.46 (0.03)	LT
57598.72	–	–	15.20 (0.04)	15.08 (0.06)	–	LCOGT
57599.70	–	–	15.24 (0.04)	15.09 (0.06)	–	LCOGT
57601.14	18.92 (0.07)	16.40 (0.03)	15.25 (0.04)	15.14 (0.03)	–	NOT
57604.99	–	–	15.37 (0.04)	15.24 (0.06)	–	LCOGT
57607.06	–	–	15.38 (0.09)	–	–	LCOGT
57609.00	19.20 (0.09)	16.41 (0.09)	15.44 (0.10)	15.29 (0.09)	14.73 (0.15)	1.82
57610.68	–	–	15.50 (0.04)	15.29 (0.06)	–	LCOGT
57612.65	–	–	15.52 (0.04)	15.37 (0.06)	–	LCOGT
57619.04	19.08 (0.14)	16.53 (0.09)	15.61 (0.11)	15.59 (0.08)	–	NOT
57621.27	–	–	15.68 (0.04)	15.46 (0.06)	–	LCOGT
57623.06	19.41 (0.15)	16.52 (0.12)	15.76 (0.14)	15.61 (0.11)	14.93 (0.14)	1.82
57623.29	–	–	15.69 (0.04)	15.52 (0.06)	–	LCOGT
57624.99	–	–	15.72 (0.04)	15.58 (0.06)	–	LCOGT
57625.92	19.14 (0.10)	16.63 (0.08)	15.86 (0.07)	15.78 (0.04)	15.10 (0.06)	1.82
57627.00	–	–	15.75 (0.04)	15.62 (0.06)	–	LCOGT
57628.98	–	–	15.75 (0.05)	15.59 (0.07)	–	LCOGT
57636.22	–	–	15.91 (0.04)	15.79 (0.06)	–	LCOGT
57638.63	–	–	15.94 (0.04)	15.82 (0.06)	–	LCOGT
57640.24	–	–	15.98 (0.04)	15.81 (0.06)	–	LCOGT
57644.01	19.53 (0.12)	16.91 (0.05)	16.04 (0.05)	15.93 (0.04)	15.32 (0.05)	NOT
57644.17	–	–	16.03 (0.05)	15.86 (0.08)	–	LCOGT
57650.92	–	–	16.14 (0.05)	16.00 (0.07)	–	LCOGT
57652.18	–	–	16.16 (0.04)	16.04 (0.06)	–	LCOGT
57654.83	–	–	16.20 (0.04)	16.10 (0.06)	–	LCOGT
57654.90	19.55 (0.12)	16.92 (0.10)	16.22 (0.11)	16.16 (0.05)	15.35 (0.12)	1.82
57655.11	19.71 (0.07)	17.01 (0.03)	16.20 (0.04)	16.04 (0.03)	15.43 (0.04)	NOT
57662.15	–	17.19 (0.06)	16.38 (0.04)	16.18 (0.03)	15.58 (0.03)	NOT
57663.90	–	–	16.34 (0.05)	16.31 (0.07)	–	LCOGT
57665.84	–	–	16.34 (0.04)	16.27 (0.06)	–	LCOGT
57667.86	–	–	16.33 (0.04)	16.28 (0.07)	–	LCOGT
57670.08	–	–	16.35 (0.04)	16.30 (0.06)	–	LCOGT
57672.85	–	–	16.43 (0.09)	16.34 (0.10)	–	LCOGT
57680.10	–	–	16.55 (0.04)	16.47 (0.06)	–	LCOGT
57687.84	–	–	16.58 (0.04)	16.61 (0.06)	–	LCOGT
57694.82	–	–	16.70 (0.04)	16.71 (0.06)	–	LCOGT
57699.81	–	–	16.81 (0.04)	16.85 (0.06)	–	LCOGT
57704.77	–	–	16.81 (0.05)	16.89 (0.07)	–	LCOGT
57707.79	–	–	17.11 (0.05)	16.94 (0.06)	–	LCOGT
57719.17	–	–	17.06 (0.13)	17.38 (0.29)	–	LCOGT
57727.71	–	18.08 (0.06)	17.30 (0.04)	17.20 (0.09)	17.06 (0.07)	1.82
57728.06	–	–	17.18 (0.04)	17.26 (0.07)	–	LCOGT
57728.86	20.89 (0.36)	18.34 (0.14)	17.34 (0.10)	17.32 (0.07)	17.27 (0.15)	1.82
57736.06	–	–	17.27 (0.07)	17.32 (0.10)	–	LCOGT
57906.38	–	21.38 (0.61)	19.57 (0.51)	19.98 (0.53)	–	MMT

Table A3. *UBVRI* photometry.

MJD	<i>U</i> (mag)	<i>B</i> (mag)	<i>V</i> (mag)	<i>R</i> (mag)	<i>I</i> (mag)	Instrument
57527.53	–	–	>17.43	–	–	ASA
57529.54	–	–	>17.29	–	–	ASA
57535.55	–	–	15.74 (0.07)	–	–	ASA
57535.77	15.86 (0.06)	16.51 (0.15)	15.86 (0.09)	–	–	UVOT
57536.14	–	16.30 (0.03)	15.51 (0.03)	–	–	NOT
57536.36	–	16.29 (0.04)	15.46 (0.03)	15.10 (0.04)	15.19 (0.07)	RK
57536.40	–	16.27 (0.10)	15.45 (0.06)	–	–	Gem
57537.14	–	15.88 (0.14)	15.14 (0.09)	–	–	NOT
57537.35	–	15.95 (0.04)	15.11 (0.03)	14.78 (0.04)	14.95 (0.07)	RK
57537.41	–	15.95 (0.09)	15.07 (0.06)	–	–	Gem
57538.37	–	–	14.80 (0.03)	14.51 (0.04)	14.69 (0.07)	RK
57538.39	–	15.70 (0.09)	14.80 (0.05)	–	–	Gem
57539.09	15.09 (0.05)	15.61 (0.10)	15.07 (0.06)	–	–	UVOT
57539.39	–	15.49 (0.09)	14.55 (0.05)	–	–	Gem
57539.57	–	–	14.56 (0.02)	–	–	ASA
57539.76	–	15.42 (0.09)	14.50 (0.08)	–	–	WHO
57540.76	–	15.27 (0.08)	14.28 (0.06)	–	–	WHO
57541.21	14.84 (0.11)	15.16 (0.08)	14.08 (0.06)	–	–	NOT
57541.36	–	15.18 (0.04)	14.21 (0.03)	14.01 (0.04)	14.24 (0.06)	RK
57541.40	–	15.18 (0.09)	14.19 (0.05)	–	–	Gem
57541.75	–	15.14 (0.09)	14.14 (0.07)	–	–	WHO
57542.36	–	15.09 (0.04)	14.07 (0.03)	13.88 (0.04)	14.14 (0.07)	RK
57542.38	–	15.05 (0.05)	14.06 (0.04)	–	–	DEM
57542.61	14.69 (0.06)	15.01 (0.06)	14.09 (0.05)	–	–	UVOT
57543.37	–	15.00 (0.09)	13.96 (0.06)	–	–	Gem
57543.41	–	14.96 (0.04)	13.93 (0.04)	–	–	DEM
57543.97	14.68 (0.06)	14.93 (0.06)	13.94 (0.05)	–	–	UVOT
57544.37	–	14.91 (0.09)	13.85 (0.06)	–	–	Gem
57544.44	–	14.90 (0.04)	13.83 (0.04)	–	–	DEM
57544.57	–	–	13.90 (0.02)	–	–	ASA
57545.34	–	14.86 (0.05)	13.78 (0.04)	–	–	DEM
57545.39	–	14.87 (0.09)	13.76 (0.06)	–	–	Gem
57545.94	14.74 (0.05)	14.87 (0.06)	13.81 (0.04)	–	–	UVOT
57546.39	–	14.84 (0.09)	13.73 (0.07)	–	–	Gem
57546.43	–	14.84 (0.05)	13.79 (0.05)	–	–	LCOGT
57546.44	–	14.82 (0.04)	13.73 (0.04)	–	–	DEM
57547.33	–	14.83 (0.04)	13.71 (0.04)	–	–	DEM
57547.37	–	14.85 (0.09)	13.72 (0.06)	–	–	Gem
57547.47	14.86 (0.06)	14.82 (0.06)	13.73 (0.04)	–	–	UVOT
57549.31	14.98 (0.06)	14.85 (0.06)	13.71 (0.05)	–	–	UVOT
57549.43	–	14.85 (0.06)	13.71 (0.03)	–	–	LCOGT
57549.50	–	–	13.76 (0.02)	–	–	ASA
57550.41	–	14.89 (0.06)	13.74 (0.03)	–	–	LCOGT
57550.58	15.04 (0.06)	14.85 (0.06)	13.62 (0.04)	–	–	UVOT
57551.42	–	14.89 (0.04)	13.68 (0.04)	–	–	DEM
57552.18	–	14.88 (0.11)	13.61 (0.14)	–	–	NOT
57552.35	–	14.96 (0.09)	13.72 (0.05)	–	–	Gem
57552.40	15.14 (0.06)	14.94 (0.06)	13.69 (0.05)	–	–	UVOT
57553.19	–	14.98 (0.07)	13.73 (0.07)	–	–	NOT
57553.35	–	15.01 (0.09)	13.75 (0.05)	–	–	Gem

Table A3. *Continued: UBVR photometry.*

MJD	<i>U</i> (mag)	<i>B</i> (mag)	<i>V</i> (mag)	<i>R</i> (mag)	<i>I</i> (mag)	Instrument
57553.37	–	14.99 (0.04)	13.74 (0.04)	–	–	DEM
57554.20	15.45 (0.06)	15.05 (0.06)	13.73 (0.05)	–	–	UVOT
57554.30	–	15.09 (0.05)	13.77 (0.04)	13.47 (0.05)	13.68 (0.08)	RK
57554.42	–	15.05 (0.04)	13.76 (0.04)	–	–	DEM
57555.34	–	15.12 (0.04)	13.82 (0.03)	13.46 (0.05)	13.63 (0.07)	RK
57555.56	15.55 (0.06)	15.07 (0.06)	13.78 (0.04)	–	–	UVOT
57556.37	–	15.18 (0.10)	13.87 (0.06)	–	–	Gem
57557.03	–	15.06 (0.08)	13.89 (0.05)	–	–	1.82
57557.34	–	15.28 (0.10)	13.99 (0.15)	13.52 (0.12)	13.60 (0.16)	JB
57557.43	–	15.29 (0.06)	13.89 (0.04)	–	–	LCOGT
57557.75	15.88 (0.07)	15.32 (0.07)	13.90 (0.05)	–	–	UVOT
57558.40	–	15.38 (0.08)	13.98 (0.09)	–	–	LCOGT
57558.45	–	–	13.97 (0.02)	–	–	ASA
57559.44	–	15.51 (0.06)	14.03 (0.03)	–	–	LCOGT
57560.57	16.24 (0.07)	15.62 (0.08)	14.08 (0.05)	–	–	UVOT
57561.52	–	–	14.16 (0.03)	–	–	ASA
57562.06	–	15.77 (0.11)	14.28 (0.11)	–	–	1.82
57562.40	–	15.78 (0.09)	14.21 (0.05)	–	–	LCOGT
57563.43	–	15.85 (0.06)	14.25 (0.04)	–	–	LCOGT
57566.23	16.90 (0.09)	16.07 (0.10)	14.49 (0.05)	–	–	UVOT
57566.33	–	16.05 (0.04)	14.46 (0.04)	13.83 (0.04)	13.89 (0.07)	RK
57566.41	–	16.11 (0.06)	14.47 (0.03)	–	–	LCOGT
57567.40	–	16.19 (0.06)	14.55 (0.03)	–	–	LCOGT
57568.40	–	16.25 (0.07)	14.60 (0.03)	–	–	LCOGT
57568.53	–	–	14.64 (0.02)	–	–	ASA
57569.38	–	16.29 (0.10)	14.55 (0.13)	13.97 (0.13)	13.81 (0.17)	JB
57569.42	–	16.18 (0.04)	14.65 (0.02)	–	–	GS
57570.43	–	–	14.77 (0.03)	–	–	ASA
57572.28	–	16.39 (0.05)	14.79 (0.03)	14.08 (0.04)	14.05 (0.07)	RK
57572.98	–	–	14.83 (0.04)	–	–	LCOGT
57572.98	17.45 (0.16)	16.45 (0.12)	14.92 (0.07)	–	–	UVOT
57573.02	–	16.46 (0.13)	14.81 (0.14)	–	–	NOT
57573.35	–	16.55 (0.08)	14.80 (0.12)	14.16 (0.12)	14.03 (0.16)	JB
57574.35	–	16.44 (0.05)	14.90 (0.03)	–	–	GS
57574.52	–	–	14.92 (0.03)	–	–	ASA
57575.29	–	16.50 (0.06)	14.92 (0.13)	14.22 (0.22)	14.14 (0.16)	RK
57575.44	–	16.67 (0.13)	14.91 (0.14)	14.25 (0.13)	14.09 (0.19)	JB
57576.09	–	16.69 (0.08)	15.00 (0.04)	–	–	LCOGT
57576.77	17.58 (0.14)	16.48 (0.12)	15.04 (0.06)	–	–	UVOT
57577.13	–	–	15.04 (0.04)	–	–	LCOGT
57577.54	–	–	15.09 (0.03)	–	–	ASA
57578.13	–	–	15.07 (0.04)	–	–	LCOGT
57578.73	17.72 (0.15)	16.65 (0.13)	15.19 (0.06)	–	–	UVOT
57579.14	–	–	15.09 (0.04)	–	–	LCOGT
57580.06	–	–	15.17 (0.04)	–	–	LCOGT
57580.33	–	16.69 (0.09)	15.12 (0.13)	14.40 (0.12)	14.18 (0.17)	JB
57580.50	–	–	15.23 (0.03)	–	–	ASA
57581.13	–	16.80 (0.07)	15.19 (0.04)	–	–	LCOGT

Table A3. *Continued: UVRI photometry.*

MJD	<i>U</i> (mag)	<i>B</i> (mag)	<i>V</i> (mag)	<i>R</i> (mag)	<i>I</i> (mag)	Instrument
57581.30	17.59 (0.14)	16.74 (0.14)	15.20 (0.06)	–	–	UVOT
57582.13	–	16.85 (0.07)	15.24 (0.04)	–	–	LCOGT
57582.34	–	16.77 (0.10)	15.22 (0.13)	14.49 (0.13)	14.28 (0.17)	JB
57583.13	–	–	15.28 (0.04)	–	–	LCOGT
57583.27	–	16.66 (0.06)	15.24 (0.06)	14.47 (0.25)	14.25 (0.15)	RK
57583.42	–	–	15.38 (0.04)	–	–	ASA
57583.45	–	16.70 (0.04)	15.25 (0.03)	–	–	GS
57584.11	–	–	15.28 (0.04)	–	–	LCOGT
57585.29	–	16.84 (0.06)	15.34 (0.04)	–	–	LCOGT
57586.13	–	–	15.42 (0.06)	–	–	LCOGT
57586.57	17.90 (0.16)	16.84 (0.16)	15.41 (0.06)	–	–	UVOT
57587.34	–	16.80 (0.11)	15.40 (0.06)	–	–	LCOGT
57587.41	–	–	15.38 (0.06)	–	–	ASA
57587.42	–	16.73 (0.05)	15.39 (0.03)	–	–	GS
57589.39	–	16.88 (0.06)	15.42 (0.04)	–	–	GS
57590.10	–	16.86 (0.09)	15.37 (0.09)	–	–	NOT
57590.15	17.77 (0.14)	16.90 (0.17)	15.53 (0.07)	–	–	UVOT
57591.32	–	16.80 (0.09)	15.49 (0.06)	–	–	LCOGT
57591.41	–	–	15.47 (0.03)	–	–	GS
57593.07	–	16.82 (0.07)	15.55 (0.05)	–	–	T50
57594.05	–	16.92 (0.06)	15.61 (0.10)	–	–	T50
57594.33	–	16.90 (0.06)	15.49 (0.14)	14.83 (0.14)	14.63 (0.17)	JB
57594.54	17.83 (0.15)	16.95 (0.17)	15.63 (0.07)	–	–	UVOT
57594.70	–	17.01 (0.08)	15.53 (0.04)	–	–	LCOGT
57595.46	–	–	15.65 (0.05)	–	–	ASA
57596.07	–	16.82 (0.15)	15.49 (0.13)	–	–	T50
57597.06	–	16.95 (0.06)	15.57 (0.08)	–	–	T50
57597.29	–	17.11 (0.08)	15.56 (0.12)	14.87 (0.13)	14.69 (0.17)	JB
57597.41	–	–	15.65 (0.04)	–	–	ASA
57597.73	–	–	15.61 (0.04)	–	–	LCOGT
57598.26	–	17.07 (0.09)	15.57 (0.13)	14.88 (0.13)	14.69 (0.17)	JB
57598.72	–	16.86 (0.06)	15.67 (0.04)	–	–	LCOGT
57598.77	–	16.91 (0.16)	15.71 (0.10)	–	–	UVOT
57599.70	–	17.00 (0.07)	15.65 (0.04)	–	–	LCOGT
57600.24	–	17.11 (0.06)	15.66 (0.11)	14.95 (0.10)	14.76 (0.15)	JB
57601.13	–	17.07 (0.07)	15.66 (0.04)	–	–	NOT
57601.44	–	–	15.77 (0.04)	–	–	ASA
57603.62	18.24 (0.26)	17.11 (0.20)	15.83 (0.08)	–	–	UVOT
57604.31	–	17.12 (0.04)	15.68 (0.09)	15.15 (0.09)	14.83 (0.14)	JB
57604.53	–	–	15.75 (0.04)	–	–	ASA
57604.99	–	–	15.82 (0.04)	–	–	LCOGT
57606.84	–	17.11 (0.18)	15.90 (0.10)	–	–	UVOT
57607.06	–	–	15.74 (0.12)	–	–	LCOGT
57607.50	–	–	15.85 (0.05)	–	–	ASA
57608.47	–	17.11 (0.18)	15.95 (0.10)	–	–	UVOT
57609.00	–	16.95 (0.09)	15.84 (0.09)	–	–	1.82
57609.24	–	17.12 (0.08)	15.71 (0.15)	15.19 (0.18)	14.80 (0.13)	RK
57610.35	–	–	15.91 (0.02)	–	–	GS
57610.37	–	–	15.80 (0.05)	–	–	ASA
57610.68	–	–	15.88 (0.04)	–	–	LCOGT

Table A3. *Continued: UBVR photometry.*

MJD	<i>U</i> (mag)	<i>B</i> (mag)	<i>V</i> (mag)	<i>R</i> (mag)	<i>I</i> (mag)	Instrument
57611.53	–	–	15.97 (0.05)	–	–	ASA
57612.40	–	17.16 (0.05)	15.89 (0.01)	–	–	GS
57612.65	–	–	15.91 (0.04)	–	–	LCOGT
57613.20	–	17.17 (0.06)	15.78 (0.11)	15.24 (0.24)	14.90 (0.18)	RK
57613.31	–	–	15.90 (0.06)	–	–	ASA
57613.51	17.96 (0.21)	17.26 (0.20)	15.94 (0.10)	–	–	UVOT
57614.36	–	17.07 (0.05)	15.91 (0.03)	–	–	GS
57614.56	–	–	15.87 (0.05)	–	–	ASA
57615.28	–	–	16.09 (0.10)	–	–	ASA
57615.74	18.29 (0.22)	17.27 (0.21)	15.97 (0.09)	–	–	UVOT
57618.48	–	–	15.97 (0.12)	–	–	ASA
57619.04	–	17.21 (0.07)	16.13 (0.07)	–	–	NOT
57621.27	–	17.12 (0.07)	16.03 (0.04)	–	–	LCOGT
57623.05	–	17.23 (0.09)	16.02 (0.12)	–	–	1.82
57623.29	–	–	16.09 (0.04)	–	–	LCOGT
57624.99	–	17.24 (0.07)	16.09 (0.04)	–	–	LCOGT
57625.92	–	17.02 (0.09)	16.14 (0.06)	–	–	1.82
57626.53	–	–	16.07 (0.06)	–	–	ASA
57627.00	–	–	16.12 (0.04)	–	–	LCOGT
57627.28	–	17.30 (0.21)	16.20 (0.10)	–	–	UVOT
57628.98	–	–	16.23 (0.06)	–	–	LCOGT
57629.64	18.34 (0.31)	17.55 (0.26)	16.24 (0.11)	–	–	UVOT
57630.48	–	–	16.33 (0.07)	–	–	ASA
57632.00	–	17.12 (0.19)	16.36 (0.15)	–	–	UVOT
57634.24	–	17.26 (0.17)	16.10 (0.11)	15.54 (0.13)	15.31 (0.07)	RK
57635.08	–	–	16.36 (0.08)	–	–	ASA
57636.08	–	–	16.25 (0.09)	–	–	ASA
57636.22	–	–	16.28 (0.04)	–	–	LCOGT
57636.28	18.40 (0.24)	17.47 (0.24)	16.38 (0.11)	–	–	UVOT
57637.50	–	–	16.36 (0.07)	–	–	ASA
57638.63	–	17.33 (0.07)	16.30 (0.04)	–	–	LCOGT
57639.40	–	–	16.35 (0.06)	–	–	ASA
57640.24	–	–	16.35 (0.04)	–	–	LCOGT
57642.16	–	–	16.29 (0.14)	–	–	ASA
57643.52	18.10 (0.18)	17.52 (0.26)	16.57 (0.12)	–	–	UVOT
57644.00	–	17.58 (0.06)	16.45 (0.05)	–	–	NOT
57644.17	–	17.11 (0.11)	16.36 (0.06)	–	–	LCOGT
57650.36	–	–	–	–	–	UVOT
57650.41	–	–	16.68 (0.13)	–	–	ASA
57650.92	–	–	16.53 (0.06)	–	–	LCOGT
57652.18	–	17.63 (0.85)	16.55 (0.04)	–	–	LCOGT
57654.83	–	17.63 (0.09)	16.60 (0.04)	–	–	LCOGT
57654.90	–	17.32 (0.10)	16.53 (0.06)	–	–	1.82
57655.04	–	–	16.61 (0.10)	–	–	ASA
57655.11	–	17.63 (0.04)	16.50 (0.03)	–	–	NOT
57656.22	–	17.49 (0.10)	16.89 (0.14)	15.94 (0.20)	15.65 (0.13)	RK
57657.35	–	–	16.68 (0.07)	–	–	ASA
57657.96	18.66 (0.50)	17.56 (0.26)	16.87 (0.21)	–	–	UVOT
57660.11	–	–	16.62 (0.10)	–	–	ASA
57660.83	–	17.79 (0.31)	16.80 (0.15)	–	–	UVOT

Table A3. *Continued: UBVR photometry.*

MJD	<i>U</i> (mag)	<i>B</i> (mag)	<i>V</i> (mag)	<i>R</i> (mag)	<i>I</i> (mag)	Instrument
57662.15	–	17.73 (0.08)	16.70 (0.03)	–	–	NOT
57662.69	18.81 (0.31)	17.84 (0.33)	16.93 (0.15)	–	–	UVOT
57663.90	–	–	16.75 (0.06)	–	–	LCOGT
57665.84	–	17.96 (0.09)	16.77 (0.04)	–	–	LCOGT
57667.42	–	–	16.80 (0.11)	–	–	ASA
57667.86	–	17.85 (0.10)	16.75 (0.05)	–	–	LCOGT
57668.33	–	–	17.00 (0.10)	–	–	ASA
57670.08	–	17.81 (0.07)	16.81 (0.04)	–	–	LCOGT
57671.29	–	–	16.96 (0.18)	–	–	ASA
57671.53	18.66 (0.29)	17.93 (0.35)	17.15 (0.19)	–	–	UVOT
57672.85	–	17.76 (0.21)	16.95 (0.13)	–	–	LCOGT
57675.22	–	–	16.90 (0.20)	–	–	ASA
57678.36	–	–	17.25 (0.27)	–	–	ASA
57680.10	–	17.94 (0.09)	16.98 (0.05)	–	–	LCOGT
57680.26	–	–	17.10 (0.10)	–	–	ASA
57681.37	18.81 (0.29)	18.14 (0.43)	17.13 (0.17)	–	–	UVOT
57687.36	–	–	17.17 (0.14)	–	–	ASA
57687.84	–	18.03 (0.07)	17.09 (0.04)	–	–	LCOGT
57690.35	–	–	17.03 (0.09)	–	–	ASA
57691.39	19.35 (0.45)	18.36 (0.53)	17.41 (0.21)	–	–	UVOT
57692.26	–	–	16.96 (0.10)	–	–	ASA
57694.82	–	18.14 (0.08)	17.20 (0.05)	–	–	LCOGT
57695.34	–	–	17.39 (0.15)	–	–	ASA
57697.33	–	–	17.11 (0.12)	–	–	ASA
57699.81	–	18.32 (0.08)	17.36 (0.05)	–	–	LCOGT
57702.25	–	–	17.61 (0.23)	–	–	ASA
57702.88	–	18.57 (0.62)	17.52 (0.23)	–	–	UVOT
57704.77	–	18.43 (0.16)	17.30 (0.08)	–	–	LCOGT
57707.21	–	–	17.78 (0.33)	–	–	ASA
57707.79	–	18.66 (0.09)	17.73 (0.06)	–	–	LCOGT
57710.21	–	–	17.35 (0.12)	–	–	ASA
57711.22	18.93 (0.34)	18.58 (0.61)	17.69 (0.27)	–	–	UVOT
57715.05	–	–	17.60 (0.23)	–	–	ASA
57718.26	–	–	18.04 (0.27)	–	–	ASA
57719.17	–	–	17.59 (0.77)	–	–	LCOGT
57721.26	–	–	18.15 (0.27)	–	–	ASA
57723.42	19.26 (0.45)	18.98 (0.60)	17.98 (0.60)	–	–	UVOT
57727.71	–	18.77 (0.06)	17.71 (0.07)	–	–	1.82
57728.06	–	18.68 (0.09)	17.87 (0.06)	–	–	LCOGT
57728.85	–	18.60 (0.10)	17.81 (0.10)	–	–	1.82
57730.81	–	18.93 (0.81)	18.02 (0.36)	–	–	UVOT
57736.06	–	18.94 (0.18)	18.00 (0.11)	–	–	LCOGT
57737.19	–	–	17.45 (0.34)	–	–	ASA
57851.63	–	–	>18.17	–	–	ASA
57860.49	>19.69	>19.89	>18.99	–	–	UVOT
57870.60	–	–	>18.40	–	–	ASA
57876.58	–	–	>18.29	–	–	ASA
57880.57	–	–	>17.80	–	–	ASA
57885.55	–	–	>17.65	–	–	ASA
57893.59	–	–	>18.55	–	–	ASA

Table A4. *JHK* photometry.

MJD	<i>J</i> (mag)	<i>H</i> (mag)	<i>K</i> (mag)	Instrument
57540.17	–	13.78 (0.27)	–	LT
57542.21	–	13.55 (0.30)	–	LT
57546.29	13.33 (0.03)	13.21 (0.02)	13.14 (0.03)	REM
57547.37	13.30 (0.02)	13.12 (0.02)	13.00 (0.04)	REM
57548.38	13.26 (0.04)	13.08 (0.02)	12.94 (0.04)	REM
57549.42	13.25 (0.04)	13.09 (0.02)	12.98 (0.06)	REM
57550.44	13.12 (0.03)	13.00 (0.02)	12.86 (0.05)	REM
57551.14	13.09 (0.35)	12.97 (0.31)	12.95 (0.33)	NOT
57551.19	–	13.03 (0.27)	–	LT
57552.06	–	13.01 (0.25)	–	LT
57553.17	–	12.94 (0.29)	–	LT
57554.12	–	12.96 (0.26)	–	LT
57554.23	13.12 (0.06)	12.91 (0.03)	12.77 (0.05)	REM
57555.24	13.01 (0.01)	12.88 (0.02)	–	REM
57557.13	–	12.86 (0.25)	–	LT
57557.22	13.04 (0.03)	12.93 (0.02)	12.74 (0.09)	REM
57558.10	–	12.86 (0.29)	–	LT
57558.23	13.02 (0.06)	12.89 (0.03)	12.79 (0.12)	REM
57559.07	–	12.82 (0.30)	–	LT
57559.24	13.01 (0.01)	12.86 (0.02)	12.69 (0.02)	REM
57560.30	13.04 (0.05)	12.88 (0.02)	12.76 (0.09)	REM
57561.06	–	12.91 (0.23)	–	LT
57561.30	13.01 (0.03)	12.85 (0.02)	12.69 (0.03)	REM
57562.12	–	12.84 (0.25)	–	LT
57562.31	13.14 (0.05)	12.96 (0.04)	–	REM
57563.13	–	12.90 (0.32)	–	LT
57566.32	13.14 (0.04)	13.01 (0.02)	12.79 (0.07)	REM
57567.33	13.13 (0.03)	12.94 (0.02)	12.78 (0.04)	REM
57568.35	13.23 (0.05)	13.00 (0.02)	12.84 (0.10)	REM
57569.08	–	13.06 (0.20)	–	LT
57569.36	13.19 (0.03)	13.00 (0.03)	–	REM
57570.17	–	13.03 (0.26)	–	LT
57575.35	13.45 (0.02)	13.22 (0.02)	13.03 (0.04)	REM
57577.10	–	13.25 (0.24)	–	LT
57579.11	–	13.34 (0.20)	–	LT
57580.12	–	13.28 (0.30)	–	LT
57581.10	–	13.34 (0.27)	–	LT
57583.34	13.78 (0.05)	13.43 (0.02)	13.22 (0.06)	REM
57586.13	–	13.47 (0.29)	–	LT
57587.43	13.92 (0.04)	13.54 (0.03)	13.43 (0.05)	REM
57588.14	–	13.58 (0.23)	–	LT
57591.43	14.14 (0.04)	13.68 (0.03)	13.44 (0.06)	REM
57593.12	–	13.71 (0.23)	–	LT
57596.31	14.23 (0.04)	13.79 (0.03)	–	REM
57600.32	14.55 (0.10)	13.87 (0.05)	–	REM
57604.32	14.55 (0.06)	–	–	REM
57608.36	14.70 (0.07)	14.23 (0.04)	13.92 (0.11)	REM
57612.38	14.80 (0.05)	14.21 (0.03)	14.01 (0.14)	REM
57617.22	14.98 (0.06)	14.37 (0.04)	14.15 (0.11)	REM
57622.36	15.28 (0.05)	14.57 (0.05)	14.44 (0.20)	REM

Table A4. *Continued: JHK photometry.*

MJD	<i>J</i> (mag)	<i>H</i> (mag)	<i>K</i> (mag)	Instrument
57623.15	15.11 (0.40)	14.69 (0.34)	14.19 (0.39)	NOT
57629.11	15.47 (0.06)	14.72 (0.07)	14.70 (0.17)	REM
57634.96	–	14.80 (0.28)	–	LT
57636.95	–	14.82 (0.30)	–	LT
57638.94	–	14.89 (0.28)	–	LT
57642.93	–	15.02 (0.28)	–	LT
57650.92	–	15.17 (0.29)	–	LT
57654.96	–	15.32 (0.25)	–	LT
57657.92	–	15.42 (0.23)	–	LT
57663.93	–	15.58 (0.26)	–	LT
57666.87	–	15.58 (0.22)	–	LT
57669.88	–	15.64 (0.31)	–	LT
57672.86	–	15.69 (0.30)	–	LT
57675.84	–	15.70 (0.28)	–	LT
57678.87	–	15.87 (0.30)	–	LT
57681.88	–	15.87 (0.28)	–	LT
57689.87	–	15.97 (0.27)	–	LT
57693.83	–	16.02 (0.23)	–	LT
57700.84	–	16.15 (0.26)	–	LT
57708.86	–	16.38 (0.26)	–	LT
57711.85	–	16.33 (0.27)	–	LT
57732.87	–	16.71 (0.26)	–	LT
57856.24	–	18.56 (0.35)	–	LT
57863.21	–	>17.65	–	LT
57866.22	–	18.61 (0.35)	–	LT

Table A5. UV photometry.

MJD	<i>UV-W2</i> (mag)	<i>UV-M2</i> (mag)	<i>UV-W1</i> (mag)	Instrument
57535.77	17.74 (0.26)	17.71 (0.22)	16.74 (0.17)	UVOT
57539.09	17.11 (0.21)	17.06 (0.14)	16.07 (0.13)	UVOT
57542.61	17.01 (0.16)	17.26 (0.16)	15.88 (0.10)	UVOT
57543.98	17.02 (0.16)	17.50 (0.18)	15.98 (0.11)	UVOT
57545.94	17.25 (0.19)	17.58 (0.20)	16.08 (0.11)	UVOT
57547.47	17.31 (0.19)	17.84 (0.23)	16.28 (0.12)	UVOT
57549.32	17.37 (0.19)	18.13 (0.29)	16.45 (0.14)	UVOT
57550.58	17.43 (0.21)	18.04 (0.27)	16.45 (0.14)	UVOT
57552.40	17.75 (0.25)	18.46 (0.37)	16.49 (0.14)	UVOT
57554.20	17.81 (0.26)	18.39 (0.35)	16.78 (0.17)	UVOT
57555.56	17.91 (0.28)	18.38 (0.38)	17.04 (0.20)	UVOT
57557.75	18.20 (0.34)	–	17.20 (0.22)	UVOT
57560.58	18.37 (0.40)	19.33 (0.76)	17.47 (0.27)	UVOT
57569.56	19.09 (0.69)	–	18.74 (0.74)	UVOT
57579.06	>19.50	>19.22	>18.85	UVOT
57588.37	–	>19.67	>18.91	UVOT
57592.35	>19.70	–	–	UVOT
57596.65	–	>19.18	>18.87	UVOT
57603.62	>19.59	>19.52	>19.18	UVOT
57612.13	>19.83	>19.53	>18.93	UVOT
57619.20	–	–	>19.23	UVOT
57631.56	>19.75	>19.81	>19.32	UVOT
57646.94	>19.88	>19.73	>19.31	UVOT
57659.40	>19.85	>19.81	>19.28	UVOT
57668.01	>19.85	>19.80	>19.35	UVOT
57681.37	>20.10	>19.94	>19.56	UVOT
57691.39	>20.14	>19.98	>19.62	UVOT
57707.04	>20.11	>19.90	>19.54	UVOT
57726.19	>19.90	>19.89	>19.43	UVOT
57860.49	>20.29	>20.08	>19.76	UVOT

Table A6. Peak time and peak magnitudes of SN 2016coi in all filters. The errors reported are the statistical error on the identification of the maxima, and do not include the uncertainties on the discovery (MJD 57535.55) and explosion date (MJD 57531.9).

Band	MJD max	Phase max [d]		Mag max
		(from disc.)	(from expl.)	
<i>UV-W2</i>	57541.50 ± 4.13	5.95	9.60	16.99 ± 0.17
<i>UV-M2</i>	57540.13 ± 4.34	4.58	8.23	17.01 ± 0.98
<i>UV-W1</i>	57542.01 ± 0.95	6.46	10.11	15.90 ± 0.07
<i>u</i>	57543.51 ± 0.52	7.96	11.61	15.61 ± 0.02
<i>U</i>	57543.85 ± 2.21	8.30	11.95	14.68 ± 0.06
<i>B</i>	57547.87 ± 0.50	12.32	15.97	14.83 ± 0.02
<i>g</i>	57548.85 ± 2.83	13.30	16.95	14.15 ± 0.09
<i>V</i>	57550.24 ± 0.16	14.69	18.34	17.86 ± 0.01
<i>r</i>	57551.88 ± 0.36	16.33	19.98	13.59 ± 0.01
<i>R</i>	57551.10 ± 0.60	15.55	19.20	13.41 ± 0.04
<i>i</i>	57554.38 ± 0.86	18.83	22.48	13.93 ± 0.02
<i>I</i>	57553.54 ± 2.26	17.99	21.64	13.63 ± 0.06
<i>z</i>	57555.50 ± 0.67	19.95	23.60	13.58 ± 0.01
<i>J</i>	57558.74 ± 0.84	23.19	26.84	13.03 ± 0.03
<i>H</i>	57562.30 ± 2.75	26.75	30.40	12.85 ± 0.09
<i>K</i>	57560.88 ± 2.13	25.33	28.98	12.72 ± 0.03

Table A7. Telescopes, instruments and configurations used for the spectroscopic follow-up of SN 2016coi.

Telescope	Instrument	Grism/Grating	Slit	Resolution [R]	Wavelength range
1.22m Galileo	B&C spectrograph	300 ln/mm	3.93''	636	3800 – 8000 Å
		Gr#4		363	3360 – 7740 Å
1.82m Copernico	AFOSC	VPH6	1.69''	300	4500 – 10000 Å
		VPH7		375	3200 – 7300 Å
du Pont Telescope	B&C spectrograph	300 ln/mm	2.71''	1667	3300 – 9500 Å
Large Binocular Telescope (LBT)	MODS	Red	0.6''	2300	5500 – 10500 Å
		Blue		1850	3200 – 6000 Å
Magellan	IMACS	300 ln/mm	0.9''	1100	3650 – 9740 Å
		VPH-Blue	1.2''	1600	3900 – 6800 Å
MDM Hiltner 2.4 m	OSMOS	VPH-Red	1.0''	1600	3920 – 9050 Å
			1.2''	1500	5350 – 10500 Å
Multiple Mirror Telescope (MMT)	Blue Channel	300 ln/mm	1.0''	750	3300 – 8600 Å
LT	SPRAT	Blue	1.8''	350	4000 – 8000 Å
NOT	ALFOSC	Gr#4	1.0''	360	3200 – 9600 Å
Tillinghast 1.5m (FLWO)	FAST	300 ln/mm	3.0''	900	3530 – 7470 Å
TNG	DOLORES	LR-B	1.0''	585	3000 – 8430 Å
		LR-R		714	4470 – 10070 Å

Table A8. Spectroscopic log.

Date obs.	MJD	Tel.+Inst.	Slit	Grism/Grating
2016-05-28	57536.2	NOT+ALFOSC	1.0''	Gr#4
2016-05-28	57536.2	LT+SPRAT	1.8''	Blue
2016-05-29	57537.2	LT+SPRAT	1.8''	Blue
2016-05-29	57537.1	NOT+ALFOSC	1.0''	Gr#4
2016-05-31	57539.4	MDM+OSMOS	1.2''	VPH-Blue
2016-06-01	57540.1	LT+SPRAT	1.8''	Blue
2016-06-02	57541.4	Till+FAST	3.0''	300 ln/mm
2016-06-02	57541.4	MDM+OSMOS	1.2''	VPH-Blue
2016-06-03	57542.5	Till+FAST	3.0''	300 ln/mm
2016-06-04	57543.4	Till+FAST	3.0''	300 ln/mm
2016-06-05	57544.5	Till+FAST	3.0''	300 ln/mm
2016-06-06	57545.4	Till+FAST	3.0''	300 ln/mm
2016-06-07	57546.2	NOT+ALFOSC	1.0''	Gr#4
2016-06-08	57547.4	Till+FAST	3.0''	300 ln/mm
2016-06-09	57548.5	Till+FAST	3.0''	300 ln/mm
2016-06-10	57549.2	LT+SPRAT	1.8''	Blue
2016-06-12	57551.2	LT+SPRAT	1.8''	Blue
2016-06-13	57552.2	NOT+ALFOSC	1.0''	Gr#4
2016-06-14	57553.1	LT+SPRAT	1.8''	Blue
2016-06-14	57553.4	LBT+MODS	0.6''	Red+Blue
2016-06-15	57554.1	LT+SPRAT	1.8''	Blue
2016-06-18	57557.0	1.82+AFOSC	1.69''	VHP6+VPH7
2016-06-19	57558.1	LT+SPRAT	1.8''	Blue
2016-06-22	57561.1	LT+SPRAT	1.8''	Blue
2016-06-23	57562.0	1.82+AFOSC	1.69''	VHP6+VPH7
2016-06-23	57562.1	LT+SPRAT	1.8''	Blue
2016-06-24	57563.1	LT+SPRAT	1.8''	Blue
2016-06-26	57565.0	LT+SPRAT	1.8''	Blue
2016-07-02	57571.2	LT+SPRAT	1.8''	Blue
2016-07-05	57574.4	Till+FAST	3.0''	300 ln/mm
2016-07-07	57576.1	1.22+B&C	3.93''	300 ln/mm
2016-07-10	57579.4	Till+FAST	3.0''	300 ln/mm
2016-07-10	57579.3	MMT+Blue Channel	1.0''	300 ln/mm
2016-07-12	57581.1	LT+SPRAT	1.8''	Blue
2016-07-17	57586.1	LT+SPRAT	1.8''	Blue
2016-07-18	57587.0	LT+SPRAT	1.8''	Blue
2016-07-21	57590.1	NOT+ALFOSC	1.0''	Gr#4
2016-07-26	57596.0	LT+SPRAT	1.8''	Blue
2016-08-01	57601.1	NOT+ALFOSC	1.0''	Gr#4
2016-08-09	57609.0	1.82+AFOSC	1.69''	VHP6+VPH7
2016-08-12	57613.0	TNG+LRS	1.0''	LR-B+LT-R
2016-08-22	57623.0	1.82+AFOSC	1.69''	VHP6+VPH7
2016-08-24	57624.0	LT+SPRAT	1.8''	Blue
2016-08-25	57625.9	1.82+AFOSC	1.69''	VHP6+Gr#4
2016-09-03	57634.8	1.82+AFOSC	1.69''	VHP6+VPH7
2016-09-03	57635.0	LT+SPRAT	1.8''	Blue
2016-09-08	57639.1	du Pont+B&C	2.71''	300 ln/mm
2016-09-16	57647.9	LT+SPRAT	1.8''	Blue
2016-09-23	57654.9	1.82+AFOSC	1.69''	VHP6+VPH7

Table A8. *Continued:* Spectroscopic log.

Date obs.	MJD	Tel.+Inst.	Slit	Grism/Grating
2016-09-24	57655.1	NOT+ALFOSC	1.0''	Gr#4
2016-09-30	57662.0	LT+SPRAT	1.8''	Blue
2016-10-01	57662.1	NOT+ALFOSC	1.0''	Gr#4
2016-10-11	57672.9	LT+SPRAT	1.8''	Blue
2016-10-13	57674.8	LT+SPRAT	1.8''	Blue
2016-11-02	57694.1	LBT+MODS	0.6''	Red+Blue
2016-11-01	57693.9	LT+SPRAT	1.8''	Blue
2016-11-15	57707.8	MDM+OSMOS	1.2''	VPH-Red
2016-11-18	57710.8	LT+SPRAT	1.8''	Blue
2016-12-05	57727.7	1.82+AFOSC	1.69''	VHP6+VPH7
2016-12-06	57728.8	1.82+AFOSC	1.69''	VHP6+VPH7
2016-12-10	57732.8	LT+SPRAT	1.8''	Blue
2017-06-17	57921.8	MDM+OSMOS	1.0''	VPH-Red
2017-06-28	57932.4	MMT+Blue Channel	1.0''	300 ln/mm
2017-07-20	57954.2	Magellan+IMACS	0.9''	300ln/mm

Table A9. Radio observations of SN 2016coi.

Start Date (UT)	Time since First Light (days)	Frequency (GHz)	Flux Density (mJy)	Project	
2016-06-03	11	5.95	2.048	1.15 ± 0.06	16A-477
2016-06-03	11	9.80	2.048	3.4 ± 0.2	16A-477
2016-06-03	11	14.75	2.048	8.9 ± 0.4	16A-477
2016-06-03	11	21.85	2.048	21 ± 1	16A-477
2016-06-13	21	5.95	2.048	4.8 ± 0.2	16A-477
2016-06-13	21	9.80	2.048	11.3 ± 0.6	16A-477
2016-06-13	21	14.75	2.048	20 ± 1	16A-477
2016-06-13	21	21.85	2.048	24 ± 1	16A-477
2016-07-08	46	3.00	2.048	3.5 ± 0.2	16A-477
2016-07-08	46	5.95	2.048	12.9 ± 0.6	16A-477
2016-07-08	46	9.80	2.048	20 ± 1	16A-477
2016-07-08	46	21.85	2.048	16.7 ± 0.8	16A-477
2016-09-07	106	3.00	2.048	14.7 ± 0.7	16A-477
2016-09-07	106	5.95	2.048	13.5 ± 0.7	16A-477
2016-09-07	106	9.80	2.048	9.6 ± 0.5	16A-477
2016-09-07	106	21.85	2.048	5.3 ± 0.3	16A-477
2017-02-17	270	5.50	2.048	6.2 ± 0.3	17A-167
2017-02-17	270	9.00	2.048	3.7 ± 0.2	17A-167
2017-02-25	278	3.00	2.048	10.1 ± 0.5	17A-167

Table A10. 0.3-10 keV X-ray light-curve of SN 2016coi.

MJD	Time since Explosion (days)	Time Range (days)	Count-rate ($c.s^{-1}$)	Unabsorbed Flux ($erg\ s^{-1}\ cm^{-2}$)	Instrument
57538.0	6.1	(1.8-10.0)	$(3.44 \pm 0.85) \times 10^{-3}$	$(1.44 \pm 0.36) \times 10^{-13}$	XRT
57543.4	11.5	-	-	$(1.44 \pm 0.61) \times 10^{-13}$	XMM
57545.6	13.7	(10.1-16.8)	$(2.43 \pm 0.67) \times 10^{-3}$	$(1.03 \pm 0.28) \times 10^{-13}$	XRT
57553.3	21.4	(17.9-24.0)	$(2.25 \pm 0.61) \times 10^{-3}$	$(0.95 \pm 0.25) \times 10^{-13}$	XRT
57559.4	27.5	-	-	$(0.64 \pm 0.19) \times 10^{-13}$	XMM
57626.0	94.1	(26.6-157.6)	$(7.47 \pm 0.18) \times 10^{-3}$	$(0.31 \pm 0.08) \times 10^{-13}$	XRT
57785.1	253.2	(168.9-326.9)	$< 1.54 \times 10^{-3}$	$< 0.65 \times 10^{-13}$	XRT